Nuclear Science and Techniques (2025) 36:225
https://doi.org/10.1007/s41365-025-01803-3

Space charge-driven resonant beam halo in high-intensity hadron synchrotrons

Jia-Yin Du[1,2,3] · Yao-Shuo Yuan[1,2,3] · Morteza Aslaninejad[4] · Jing-Tong Du[1,2,3] · Ming-Yang Huang[1,2,3] · Sheng Wang[1,2,3]

Received: 8 July 2024 / Revised: 16 August 2024 / Accepted: 31 August 2024 / Published online: 20 September 2025

Abstract
With the significant development of high-intensity hadron (proton and heavy ion) accelerator facilities, the space charge effect has become a major limiting factor for increasing beam intensity because it can drive particle resonance, forming beam halos and causing beam quality degradation or even beam loss. In studies on space charge, the particle-core model (PCM) has been widely adopted to describe halo particle formation. In this paper, we generalize the conventional PCM to include dispersion to investigate the physical mechanism of the beam halo in high-intensity synchrotrons. In particular, a "1:1 parametric resonance" driven by the combined effects of space charge and dispersion is identified. A large dispersion is proven to have a damping effect on the 2:1 parametric resonance. The analysis based on the generalized PCM agrees with particle-in-cell simulations. A beam halo with large mismatch oscillations is also discussed.

Keywords Particle core model · Space charge · Beam halo

1 Introduction

In recent years, an increasing number of high-intensity proton or heavy-ion accelerators have been proposed, are under construction, or have begun operate worldwide for various scientific and industrial applications. For such high-intensity accelerators, studies on the mechanism of intense beams and the control of beam losses are of key importance for machine design and operation. One of the most important contributors to beam quality degradation is the formation of a beam halo driven by space charge [1–13]. The main driven source of the beam halo is parametric resonance, which causes severe beam losses (see, for example, [14–16]). Uncontrolled beam losses can cause severe consequences such as the residual activation of beam pipes, quenching of superconducting magnets, vacuum degradation, and radiation damage to insulation materials [17–20]. One of the most widely employed approaches for studying beam halos is the particle-core model (PCM) [21–30]. Compared with particle-in-cell (PIC) simulations, the PCM method is an analytical tool for investigating beam dynamics, particularly for the mechanism of beam halo formation, without requiring much particle tracking, which can be time-consuming. In this model, the dynamic behavior of an intense beam core is described by the evolution of the beam envelopes [31, 32]. The motion of a single particle is affected by the space charge of beam–core mismatch oscillations [33–38]. This becomes more complicated for high-intensity hadron synchrotrons, where the combined effect of space charge and dispersion plays a role in the motion of circulating beams [39–43]. To analyze beam halo formation in circular machines, the conventional PCM method must be generalized to include dispersion.

This work was supported by the National Natural Science Foundation of China (No. 12475155), the GuangDong Basic and Applied Basic Research Foundation (No. 2024A1515012658) and the International Partnership Program of Chinese Academy of Sciences (No. 013GJHZ2023026FN).

✉ Yao-Shuo Yuan
ysyuan@ihep.ac.cn

[1] Institute of High Energy Physics, Chinese Academy of Sciences, Beijing 100049, China

[2] University of Chinese Academy of Sciences, Beijing 100049, China

[3] Spallation Neutron Source Science Center, Dongguan 523803, China

[4] Institute for Research in Fundamental Sciences, School of Particles and Accelerators, Tehran 19395-5531, Iran

In this paper, we investigate the dynamics of halo particles in the presence of both moderate and strong space charge, where 2:1 and higher-order resonances or even chaos exist. Furthermore, based on the generalization of the conventional PCM method to a case with the dispersion effect for high-intensity synchrotrons, a novel "1:1 parametric resonance" driven by the dispersion mode is identified. We also explain the damping effect observed by Ikegami et al. [39] from the perspective of the oscillation modes. For beams with large mismatch oscillations, we discuss the high- and low-order resonances driven by the high- and low-order beam-core oscillation modes.

The remainder of this paper is organized as follows. Following this introduction, we briefly discuss the fundamentals of the PCM method in Sect. 2. The single-particle dynamics of round and elliptical beams are investigated in Sect. 3. In Sect. 4, we generalize the PCM method to include dispersion, and the 1:1 parametric resonance driven by the dispersion mode is discussed in detail. An analysis of the high-order modes in the large beam mismatch oscillation is presented in Sect. 5. Finally, the summary is presented in Sect. 6.

2 Fundamentals

In the PCM, beams are assumed to have a uniform spatial density in the transverse plane (KV distribution) because the dynamics of a single particle are insensitive to the details of the beam-core distribution. An envelope approach is employed to describe the mismatch oscillations of the beam core. Beam halo formation is driven by the space charge interaction between the collective envelope oscillation modes and single particles.

2.1 Beam-core oscillations

Let us begin with a coasting beam propagating through a uniformly focusing structure. Such a structure can be used to describe the average dynamic behavior of beams in an alternating gradient focusing channel [31] (i.e., the smooth approximation method). For simplicity, henceforth, we neglect any impedance effects caused by the beam pipe and all the chromatic terms. We adopt x and y to represent the transverse degrees of freedom in the horizontal and vertical directions, respectively, and s the longitudinal coordinate. The "pseudo"-Hamiltonian of the beam envelope oscillation in such a transport system is

$$H_{\rm env} = \frac{1}{2}(\sigma_{px}^2 + \sigma_{py}^2 + \kappa_{x,0}^2\sigma_x^2 + \kappa_{y,0}^2\sigma_y^2) - \frac{1}{2}K_{\rm sc}\ln(\sigma_x+\sigma_y) + \frac{\varepsilon_x^2}{2\sigma_x^2} + \frac{\varepsilon_y^2}{2\sigma_y^2}, \tag{1}$$

where $\sigma_{x,y}$ represents the RMS transverse beam size (for KV beams, the total transverse beam size is $2\sigma_{x,y}$). The derivatives $\sigma_{px,py}$ are the conjugate variables $\mathrm{d}\sigma_{x,y}/\mathrm{d}s = \sigma_{px,py}$. $\kappa_{x,0}$ and $\kappa_{y,0}$ are the external transverse focusing gradients in x and y, respectively. ε_x and ε_y are the transverse RMS emittances. $K_{\rm sc}$ is the space charge perveance defined by $K_{\rm sc} = 2N_{\rm L}r_{\rm c}/(\beta^2\gamma^3)$, where $N_{\rm L}$ is the number of particles per unit length, $r_{\rm c}$ is the classical proton radius, and β and γ are relativistic factors. The RMS envelope equations can be derived from the envelope Hamiltonian in Eq. (1):

$$\begin{aligned}\frac{\mathrm{d}^2\sigma_x}{\mathrm{d}s^2} + \kappa_{x,0}^2\sigma_x - \frac{K_{\rm sc}}{2(\sigma_x+\sigma_y)} - \frac{\varepsilon_x^2}{\sigma_x^3} = 0,\\ \frac{\mathrm{d}^2\sigma_y}{\mathrm{d}s^2} + \kappa_{y,0}^2\sigma_y - \frac{K_{\rm sc}}{2(\sigma_x+\sigma_y)} - \frac{\varepsilon_y^2}{\sigma_y^3} = 0.\end{aligned} \tag{2}$$

Under constant focusing, obtaining the matched RMS beam sizes $\sigma_{x,\rm m}$ and $\sigma_{y,\rm m}$ via the corresponding algebraic equation set is straightforward:

$$\begin{aligned}\kappa_{x,0}^2\sigma_{x,\rm m} - \frac{K_{\rm sc}}{2(\sigma_{x,\rm m}+\sigma_{y,\rm m})} - \frac{\varepsilon_x^2}{\sigma_{x,\rm m}^3} = 0,\\ \kappa_{y,0}^2\sigma_{y,\rm m} - \frac{K_{\rm sc}}{2(\sigma_{x,\rm m}+\sigma_{y,\rm m})} - \frac{\varepsilon_y^2}{\sigma_{y,\rm m}^3} = 0.\end{aligned} \tag{3}$$

Here, we use the subscript "m" to denote the matched case.

The envelope equations in Eq. (2), which are typically employed to describe the oscillatory motion of the beam core, can be converted into a dimensionless form with a set of dimensionless variables, defined by

$$\begin{cases}\hat{\sigma}_x &= \sigma_x/\sigma_{x,\rm m}\\ \hat{\sigma}_y &= \sigma_y/\sigma_{x,\rm m}\\ \hat{\sigma}_{px} &= \sigma_{px}/(\kappa_{x,0}\sigma_{x,\rm m})\\ \hat{\sigma}_{py} &= \sigma_{py}/(\kappa_{x,0}\sigma_{x,\rm m})\\ \tau &= \kappa_{x,0}s\end{cases} \tag{4}$$

and the dimensionless parameters

$$\begin{cases}\mu_x &= \Delta\kappa_x^2/\kappa_{x,0}^2\\ r &= \sigma_{y,\rm m}/\sigma_{x,\rm m}\\ \eta &= \kappa_{y,0}/\kappa_{x,0}\\ \varepsilon_r &= \varepsilon_y/\varepsilon_x.\end{cases} \tag{5}$$

Here, $\Delta\kappa_x^2 = K_{\rm sc}/[2\sigma_{x,\rm m}(\sigma_{x,\rm m}+\sigma_{y,\rm m})]$ represents the space charge tuning depression in the matched case. Clearly, for constant focusing, the dimensionless matched beam sizes $\hat{\sigma}_{x,\rm m} = 1, \hat{\sigma}_{y,\rm m} = r$.

The corresponding dimensionless form of the Hamiltonian in Eq. (1) and envelope equations in Eq. (2) can be, respectively, expressed as

$$\hat{H}_{\mathrm{env}} = \frac{1}{2}(\hat{\sigma}_{\mathrm{px}}^2 + \hat{\sigma}_{\mathrm{py}}^2 + \hat{\sigma}_x^2 + \eta^2\hat{\sigma}_y^2) - \mu_x(1+r)\ln(\hat{\sigma}_x + \hat{\sigma}_y) + \frac{1-\mu_x}{2\hat{\sigma}_x^2} + \frac{\varepsilon_{\mathrm{r}}^2(1-\mu_x)}{2\hat{\sigma}_y^2}, \tag{6}$$

and

$$\begin{aligned} &\frac{\mathrm{d}^2\hat{\sigma}_x}{\mathrm{d}\tau^2} + \hat{\sigma}_x - \frac{\mu_x(1+\mathrm{r})}{(\hat{\sigma}_x+\hat{\sigma}_y)} - \frac{1-\mu_x}{\hat{\sigma}_x^3} = 0, \\ &\frac{\mathrm{d}^2\hat{\sigma}_y}{\mathrm{d}\tau^2} + \eta^2\hat{\sigma}_y - \frac{\mu_x(1+\mathrm{r})}{(\hat{\sigma}_x+\hat{\sigma}_y)} - \frac{\varepsilon_{\mathrm{r}}^2(1-\mu_x)}{\hat{\sigma}_y^3} = 0. \end{aligned} \tag{7}$$

In practice, beams are not fully matched because of magnetic errors or the misalignment of lattice elements; hence, $\{\hat{\sigma}_x, \hat{\sigma}_y\}$ differs slightly from the matched solution $\{\hat{\sigma}_{x,\mathrm{m}}, \hat{\sigma}_{y,\mathrm{m}}\}$, which is referred to as a beam-coherent mismatch oscillation. In the PCM, such mismatch oscillations provide the energy transferred from the beam core to single particles via space charge, forming halo particles when resonance occurs. A mismatched beam traveling in a constant-focusing channel can often be expressed as small perturbations $(\xi, \zeta, \xi_{\mathrm{p}}, \zeta_{\mathrm{p}})$ on the matched solutions:

$$\begin{aligned} \hat{\sigma}_x &= \hat{\sigma}_{x,\mathrm{m}} + \xi = 1 + \xi, \\ \hat{\sigma}_y &= \hat{\sigma}_{y,\mathrm{m}} + \zeta = r + \zeta, \\ \hat{\sigma}_{\mathrm{px}} &= \hat{\sigma}_{\mathrm{p}x,\mathrm{m}} + \xi_{\mathrm{p}}, \\ \hat{\sigma}_{\mathrm{py}} &= \hat{\sigma}_{\mathrm{py},\mathrm{m}} + \zeta_{\mathrm{p}}. \end{aligned} \tag{8}$$

Substituting Eq. (8) into Eq. (6), we can obtain the Hamiltonian for an envelope with perturbations:

$$\begin{aligned} \hat{H}_{\mathrm{per}} = &\frac{1}{2}\left[(\hat{\sigma}_{px,\mathrm{m}} + \xi_{\mathrm{p}})^2 + (\hat{\sigma}_{\mathrm{py},\mathrm{m}} + \zeta_p)^2 + (1+\xi)^2 + \eta^2(r+\zeta)^2\right] \\ &- \mu_x(1+r)\ln(1+r+\xi+\zeta) \\ &+ \frac{1-\mu_x}{2(1+\xi)^2} + \frac{\varepsilon_{\mathrm{r}}^2(1-\mu_x)}{2(r+\zeta)^2}. \end{aligned} \tag{9}$$

By performing Taylor expansion and maintaining the linear term, from Eq. (9), we can obtain the equations of motion for the envelope perturbations in matrix form (further discussion in Appendix A):

$$\frac{\mathrm{d}^2}{\mathrm{d}\tau^2}\begin{pmatrix}\xi\\ \zeta\end{pmatrix} = -\begin{pmatrix}a_0 & a_1\\ a_1 & a_2\end{pmatrix}\begin{pmatrix}\xi\\ \zeta\end{pmatrix} \tag{10}$$

with the coefficients

$$\begin{aligned} a_0 &= 4(1-\mu_x) + \frac{r+2}{r+1}\mu_x, \\ a_1 &= \frac{\mu_x}{r+1}, \\ a_2 &= 4(\eta^2 - \frac{\mu_x}{r}) + \frac{2r+1}{r+1}\frac{\mu_x}{r}. \end{aligned} \tag{11}$$

As the coefficient matrix in Eq. (10) is symmetric, it can be decomposed via $A = U \cdot \mathrm{diag}\{k_{\mathrm{b}}^2, k_{\mathrm{q}}^2\} \cdot U^{\mathrm{T}}$, where U is the eigenvector matrix of A. Here, k_{b} and k_{q} represent the wavenumbers of the "breathing mode" and "quadrupole mode," respectively. The general solutions to Eq. (10) can be expressed as

$$\begin{aligned} \xi(\tau) &= C_{11}\cos(k_{\mathrm{b}}\tau) + C_{12}\cos(k_{\mathrm{q}}\tau), \\ \zeta(\tau) &= C_{21}\cos(k_{\mathrm{b}}\tau) + C_{22}\cos(k_{\mathrm{q}}\tau), \end{aligned} \tag{12}$$

with the coefficients

$$C_{ij} = \sum_{k=1}^{2} U_{ij}U_{jk}^{\mathrm{T}}\alpha_k, \tag{13}$$

where the two initial values $\alpha_1 = \xi(0), \alpha_2 = \zeta(0)$. Here, we use τ defined in Eq. (4) as the independent variable, and the mismatch of the monument does not consider $(\xi_{\mathrm{p}}(0) = \zeta_{\mathrm{p}}(0) = 0)$ such that Eq. (12) does not include the "sin" term. The envelope oscillation patterns depend on the initial values. For example, a pure breathing mode exists with $\zeta(0) = -(U_{21}/\,U_{22})\xi(0)$ and a pure quadrupole mode with $\zeta(0) = -(U_{11}/\,U_{12})\xi(0)$. Generally, beam-core oscillations can be characterized by a superposition of the two modes.

2.2 Single-particle motion with space charge of beam cores

In the presence of space charge, the horizontal motion of a test particle is governed by

$$\frac{\mathrm{d}^2x}{\mathrm{d}s^2} + \kappa_{x,0}^2 x = \frac{K_{\mathrm{sc}}}{2\sigma_x(\sigma_x+\sigma_y)}x \tag{14}$$

when the particle is inside the beam core ($|x| < 2\sigma_x$), and

$$\frac{\mathrm{d}^2x}{\mathrm{d}s^2} + \kappa_{x,0}^2 x = \frac{2K_{\mathrm{sc}}}{x^2 + |x|\sqrt{x^2 + 4(\sigma_y^2 - \sigma_x^2)}}x \tag{15}$$

when the particle is outside the beam core ($|x| > 2\sigma_x$). Here, x is the horizontal displacement from the center of the beam core. Using the dimensionless parameters defined in Eqs. (4) and (5), we can convert the equation of particle motion in Eqs. (14) and (15) into

$$\frac{\mathrm{d}^2\hat{x}}{\mathrm{d}\tau^2}+\hat{x}=\frac{\mu_x(1+r)}{\hat{\sigma}_x(\hat{\sigma}_x+\hat{\sigma}_y)}\hat{x},\qquad |\hat{x}|<\hat{\sigma}_x, \tag{16}$$

and

$$\frac{\mathrm{d}^2\hat{x}}{\mathrm{d}\tau^2}+\hat{x}=\frac{\mu_x(1+r)}{\hat{x}^2+|\hat{x}|\sqrt{\hat{x}^2+(\hat{\sigma}_y^2-\hat{\sigma}_x^2)}}\hat{x},\qquad |\hat{x}|>\hat{\sigma}_x. \tag{17}$$

Here, the dimensionless horizontal displacement is defined as $\hat{x}=x/2\sigma_{x,\mathrm{m}}$. Equations (16) and (17) show that when the test particle travels inside and outside the beam core, the wavenumbers of the particles are different because of the varying space charge strength.

For particles inside the beam core, the wavenumber becomes minimum: Substituting Eqs. (8) and (12) into Eq. (16), we obtain

$$\frac{\mathrm{d}^2\hat{x}}{\mathrm{d}\tau^2}+(1-\mu_x)\hat{x}=f(\tau), \tag{18}$$

with minimum number of waves

$$k_{\mathrm{p,min}}=\sqrt{1-\mu_x}, \tag{19}$$

where $f(\tau)$ is a function that describes the oscillation of the beam core.

$$f(\tau)=-\frac{\mu_x}{1+r}\Big\{[(2+r)C_{11}+C_{21}]\cos(k_{\mathrm{b}}\tau) +[(2+r)C_{12}+C_{22}]\cos(k_{\mathrm{q}}\tau)\Big\}. \tag{20}$$

We can observe that $k_{\mathrm{p,min}}$ depends only on the space charge depression μ_x.

However, when the test particle is far from the beam core, the space charge can be neglected ($\mu_x=0$), and Eq. (17) becomes

$$\frac{\mathrm{d}^2\hat{x}}{\mathrm{d}\tau^2}+\hat{x}=0. \tag{21}$$

At this zero space charge limit, the wavenumber reaches its maximum,

$$k_{\mathrm{p,max}}=1. \tag{22}$$

Generally, for a single particle traveling outside the beam core, $\sqrt{1-\mu_x}\le k_{\mathrm{p}}\le 1$.

In the PCM , particles move periodically inside and outside the beam core. In particular, when the wavenumbers of a test particle and beam core satisfy

$$k_{\mathrm{p}}=\frac{k_{\mathrm{b,q}}}{2}, \tag{23}$$

where k_{b} and k_{q} are the wavenumbers of the "breathing mode" and "quadrupole mode," the 2:1 parametric resonance occurs and forms a beam halo [37].

To illustrate this, we plot the wavenumbers as functions of the beam current (in units of the normalized space charge tune depression μ_x defined in Eq. 5) by solving Eqs. (16) and (17) for two representative cases: round and elliptical beams. In Fig. 1, the blue dashed lines represent the two limits of the single-particle wavenumber $k_{\mathrm{p,min}}=\sqrt{1-\mu_x}$ and $k_{\mathrm{p,max}}=1$, whereas the solid lines represent half of the wavenumbers for breathing mode $k_{\mathrm{b}}/2$ and quadrupole mode $k_{\mathrm{q}}/2$.

Figure 1a shows that for round beams, $k_{\mathrm{p,min}}<k_{\mathrm{q}}/2, k_{\mathrm{b}}/2<k_{\mathrm{p,max}}$ always holds as the beam current increases from the zero space charge limit ($\mu_x=0$) to the extreme space charge limit ($\mu_x=1.0$), indicating that both envelope modes can resonate with the test particle and drive the 2:1 parametric resonance. In comparison, for the elliptical beams shown in Fig. 1b, we obtain $k_{\mathrm{p,min}}<k_{\mathrm{q}}/2, k_{\mathrm{b}}/2<k_{\mathrm{p,max}}$ when $\mu_x>0.39$, which implies that the breathing mode can drive the 2:1 parametric resonance in the range of $\mu_x>0.39$. For $\mu_x<0.39$, we have $k_{\mathrm{p,min}}<k_{\mathrm{q}}/2<k_{\mathrm{p,max}}$ and $k_{\mathrm{b}}/2>k_{\mathrm{p,max}}$. In this case, the 2:1 parametric resonance can only be driven by the quadrupole mode.

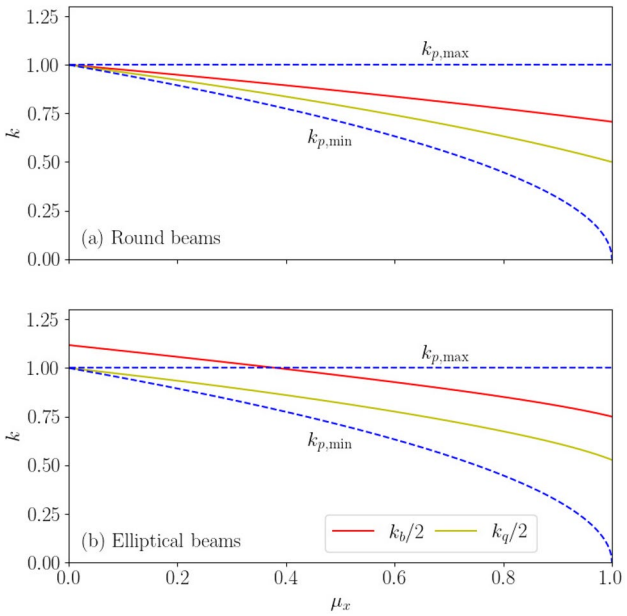

Fig. 1 (Color online) Half wavenumber of the breathing mode $k_{\mathrm{b}}/2$ (in red) and the quadrupole mode $k_{\mathrm{q}}/2$ (in yellow) versus the beam current in the unit of μ_x for round (upper panel) and elliptical beams (lower panel). The maximum ($k_{\mathrm{p,max}}$) and minimum ($k_{\mathrm{p,min}}$) wavenumbers of single particles are also plotted for comparison

3 Resonance and chaos in the beam halo

In the presence of space charge, the motion of the particles around the beam core is periodic. When resonance occurs, the particles can absorb energy from the beam core and experience a much larger contour, forming halo particles. Furthermore, particles exhibit chaotic behavior with the superposition of different modes under a strong space charge. In this section, the 2:1 and higher-order parametric resonances and chaos in the beam halo formation are investigated in detail.

3.1 Round beams in the breathing mode

Let us consider a round beam traveling in a symmetric focusing channel with initial equal mismatch perturbations on x and y, for example $\xi(0) = \zeta(0) = 0.05$, to excite a breathing mode on the beam (i.e., an in-phase pattern and 5% mismatch; the quadruple mode is absent here). We select four single particles with different initial (dimensionless) horizontal displacements, $\hat{x}_1 < 1.0 < \hat{x}_2 < \hat{x}_3 < \hat{x}_4$ (shown in Fig. 2; the dimensionless beam-core radius is 1), and the momentum is zero. By numerically solving Eqs. (16) and (17), we plot the particle motion is on a Poincaré map for the two representative cases in Fig. 2. The moderate space charge $\mu_x = 0.1$ and strong space charge $\mu_x = 0.8$ are discussed in detail below.

First , we analyze the moderate space charge case $\mu_x = 0.1$. For the two test particles with initial positions $\hat{x}_1$ and $\hat{x}_2$, the motions of the particles take the form of regular ellipses on the Poincaré map in Fig. 2a. In comparison, the third particle with initial position $\hat{x}_3$ experiences a large excursion (red trajectory), indicating that resonance appears. In this case, energy is transferred from the beam core to the particle, driving the particle to reach the largest displacement $\hat{x}_{3,\max}$.

The "lock" of the wavenumber of the third particle in Fig. 2b is a typical characteristic of the parametric resonance. Within the resonance island (red contour in Fig. 2a), the wavenumber is equal to half of the wavenumber of the breathing mode ($k = k_b/2$) in Fig. 2b. In comparison, the wavenumber increases outside the resonance region with a larger initial position ($\hat{x}_4$ in Fig. 2a, for example) when parametric resonance is absent. The lock on the half wavenumber indicates the occurrence of a 2:1 parametric resonance.

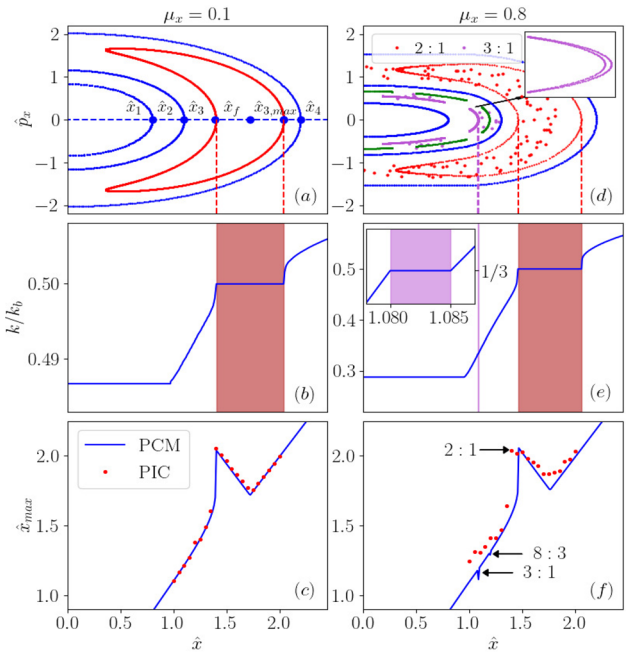

Fig. 2 (Color online) Motion of single particles with different initial positions in the presence of the breathing mode with moderate ($\mu_x = 0.1$, left column **a**, **b** and **c**) and strong space charge ($\mu_x = 0.8$, right column **d**, **e** and **f**). The Poincaré sections are shown in **a** and **d**; the wavenumber of single particle (normalized to the breathing mode) as a function of initial positions is shown in **b** and **e**; and the maximum displacement of single particle as a function of initial displacement is shown in **c** and **f** compared with the simulation results (red dotted lines)

PIC simulations were conducted using the PyORBIT code to support the above numerical results and analysis. In the simulation, a constant-focusing channel with 16 "equal cells" was employed. The main parameters used in the simulation are summarized in Table 1. The space charge solver is based on the fast Fourier transform (FFT) method [44].

Table 1 Main parameters used in the simulation

Parameters	Round beam	Elliptical beam
Length per cell (m)	14.2	14.2
Phase advance in x (deg)	108	100
Phase advance in y (deg)	108	112
RMS emit. in x (mm·mrad)	30	30
RMS emit. in y (mm·mrad)	30	30
Beam intensity (particle numbers)	1.18×10^{10} ($\mu_x = 0.1$)	1.07×10^{10} ($\mu_x = 0.1$)
	20.0×10^{10} ($\mu_x = 0.8$)	7.05×10^{10} ($\mu_x = 0.5$)
		17.5×10^{10} ($\mu_x = 0.8$)

The simulation results for the maximum displacement of the particles as a function of the initial displacement at $\mu_x = 0.1$ are shown in Fig. 2c. The simulation results were in good agreement with the numerical solutions.

Second, with an enhanced space charge ($\mu_x = 0.8$), the motion of single particles becomes more complicated, as shown in Fig. 2d–f (right). Compared with the moderate space charge case ($\mu_x = 0.1$), three small islands are observed in addition to the 2:1 resonance island in Fig. 2d. A closer examination of Fig. 2e reveals that in the region of $1.080 < \hat{x} < 1.085$, the wavenumber is locked at $k = (1/3)k_b$, indicating a 3:1 parametric resonance. Compared with the 2:1 resonance case, the small areas of the three islands indicate that the 3:1 resonance is much weaker. (The corresponding narrow stopband is shown in purple in Fig. 2e.)

PIC simulations with $\mu_x = 0.8$ were also performed. As shown in Fig. 2d, the particles were trapped within the 2:1 resonance island (shown as red dots). The purple dots around the three islands indicate that the particles gathered around the 3:1 resonance island because of the weak 3:1 resonance. The simulation results for the maximum particle displacement are shown in Fig. 2f. These results agreed with the numerical calculations.

An interesting question may be raised as to whether the 4:1 parametric resonance exists and contributes to the beam halo for a strong space charge with $\mu_x = 0.8$. As shown in Fig. 3, we obtain $k_b/4 < k_{p,min}$ when $\mu_x = 0.8$, indicating that a 4:1 or higher parametric resonance cannot be excited. In comparison, the condition $k_{p,min} < k_b/3 < 3k_b/8 < k_{p,max}$ is satisfied when $\mu_x = 0.8$, which supports the occurrence of the 3:1 and 8:3 resonance islands shown in Fig. 2.

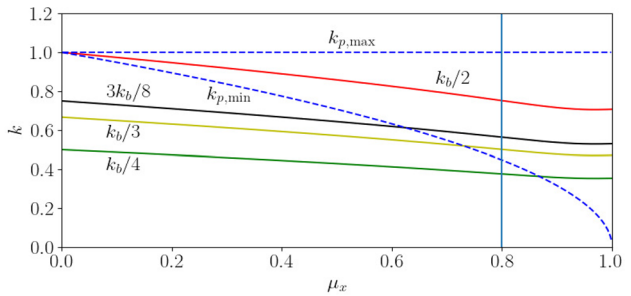

Fig. 3 (Color online) One third ($k_b/3$), one quarter ($k_b/4$), and 8:3 ($3k_b/8$) of the wavenumber of the breathing mode versus beam current in the unit of μ_x for round beams. The maximum ($k_{p,max}$) and minimum ($k_{p,min}$) wavenumber of single particles is also plotted for comparison

3.2 Round beams with mixed modes

In this subsection, we consider a round beam perturbed with $\xi(0) \neq \zeta(0)$, which can simultaneously drive both the breathing and quadrupole modes. The motion of single particles affected by the space charge of the two modes is obtained and plotted on a Poincaré map in Fig. 4, which shows that both modes can drive the 2:1 parametric resonance when the wavenumber of the test particle k satisfies $k = k_q/2$ and $k = k_b/2$, respectively.

Furthermore, a chaotic phenomenon appears in the mixed modes, as indicated by the black region in Fig. 4a and d. In contrast to the characteristic "lock of the wavenumber" of the parametric resonance, when chaos occurs, the wavenumber of the test particle is random, as shown in Fig. 4b and e.

PIC simulations were performed for the mixed modes, and the results are indicated in Fig. 4c and f using red dots. With a moderate space charge ($\mu_x = 0.1$), the simulation results for the maximum displacements agreed with the numerical calculations.

Note that the disagreement between the simulation result and numerical calculation becomes observable in the strong space charge case, as shown in Figs. 2f and 4f.

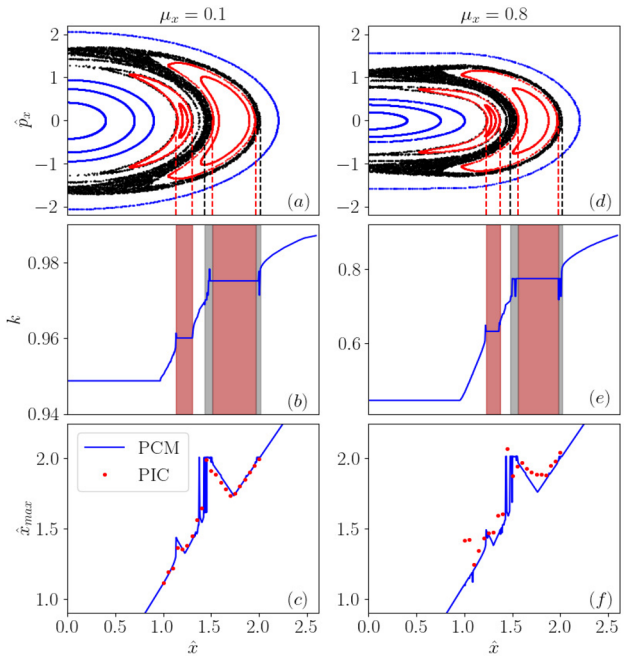

Fig. 4 (Color online) Motion of single particles with different initial positions in the presence of mixed mode with moderate ($\mu_x = 0.1$, left column **a**, **b**, and **c**) and strong space charge ($\mu_x = 0.8$, right column **d**, **e**, and **f**). The Poincaré sections are shown in **a** and **d**; the wavenumbers of single particles as functions of initial positions are shown in **b** and **e**; and the maximum displacements of single particles as functions of initial displacement are shown in **c** and **f**, compared with the simulation results (red dotted lines)

We attribute this to the disturbance of the uniform particle distribution during self-consistent particle tracking, resulting in different wavenumbers of single particles from the PCM.

3.3 Elliptical beams

In the following, we discuss the case of elliptical beams, i.e., $r \neq 1$. The wavenumbers as functions of the normalized space charge tune depression μ_x are numerically obtained and shown in Fig. 1b, where $\eta = 1.25$ and $r = 0.9$. For a moderate space charge ($\mu_x = 0.1$), only the quadrupole mode can induce the 2:1 resonance.

The motions of single particles affected by the space charge of the two modes in the elliptical beams are obtained and plotted on a Poincaré map in Fig. 5. The characteristic "lock of the wavenumber" is shown in Fig. 5b. For $\mu_x \geq 0.5$, two resonance islands appear, as shown in Fig. 5d and g, which are driven by the quadrupole and breathing modes, respectively. The locks of the two modes are shown in Fig. 5e and h. Furthermore, Fig. 5d and g shows that as space charge increases, the two resonance islands approach each other. With strong space charge ($\mu_x = 0.8$), as shown in Fig. 5g, the 2:1 resonance islands of the breathing and quadrupole modes are closer to each other, which causes chaotic phenomena around the two adjacent resonant islands (shown as black dots).

PIC simulations were performed for the mixed modes in elliptical beams using the parameters listed in Table 1. The simulation results for the maximum displacements are shown in Fig. 5c, f, and i using red points. The simulation results were in good agreement with the numerical calculations.

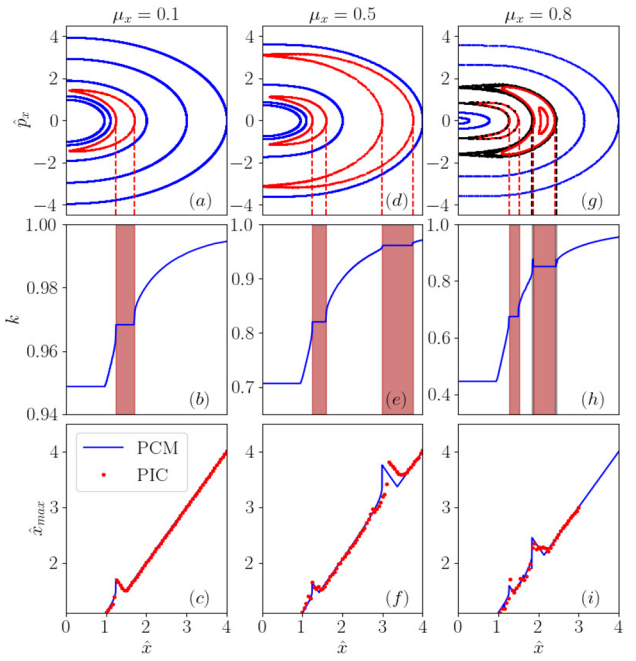

Fig. 5 (Color online) Motion of single particles with different initial positions under the mixed mode with moderate ($\mu_x = 0.1$, left column **a**, **b** and **c**), enhanced ($\mu_x = 0.5$, center column **d**, **e**, and **f**) and strong space charge ($\mu_x = 0.8$, right column **g**, **h**, and **i**). The Poincaré sections are shown in **a**, **d**, and **g**; the wavenumbers of single particles as functions of initial positions are shown in **b**, **e**, and **h**; and the maximum displacements of single particles as functions of initial displacement are shown in **c**, **f**, and **i**, compared with the simulation results (red dotted lines)

4 Beam halo formation in high-intensity synchrotrons

In this section, we investigate beam halo formation driven by the resonant interaction between single particles and the beam core in high-intensity synchrotrons, in which the combined effect of space charge and dispersion has been considered [39–43]. Hence, the conventional PCM is generalized to include dispersion. Note that the mechanism of the beam halo formation discussed here differs from space charge structural resonances, which are driven by high-order terms in the space charge potential [45–50].

4.1 Generalized PCM with dispersion

For beams traveling in a constant-focusing bending channel, the transverse beam dynamics can be described by the envelope equation set with the dispersion function, given by [2, 51]

$$\begin{aligned}
&\frac{\mathrm{d}^2}{\mathrm{d}s^2}\sigma_x + \kappa_{x,0}^2\sigma_x - \frac{K_{\mathrm{sc}}}{2X(X+Y)}\sigma_x - \frac{\varepsilon_{\mathrm{dx}}^2}{\sigma_x^3} = 0,\\
&\frac{\mathrm{d}^2}{\mathrm{d}s^2}\sigma_y + \kappa_{y,0}^2\sigma_y - \frac{K_{\mathrm{sc}}}{2Y(X+Y)}\sigma_y - \frac{\varepsilon_{\mathrm{dy}}^2}{\sigma_y^3} = 0,\\
&\frac{\mathrm{d}^2}{\mathrm{d}s^2}D_\delta + \kappa_{x,0}^2 D_\delta - \frac{K_{\mathrm{sc}}}{2X(X+Y)}D_\delta = \frac{\sigma_{\mathrm{p}}}{\rho},
\end{aligned} \tag{24}$$

which can be derived from the dispersion-modified envelope Hamiltonian:

$$H_{\mathrm{env,d}} = \frac{1}{2}(\sigma_{\mathrm{px}}^2 + \sigma_{\mathrm{py}}^2 + D_{\mathrm{p}\delta}^2) + V_{\mathrm{env,d}}(\sigma_x, \sigma_y, D_\delta) \tag{25}$$

with

$$\begin{aligned}
V_{\mathrm{env,d}}(\sigma_x, \sigma_y, D_\delta) = &\frac{1}{2}\kappa_{x,0}^2\sigma_x^2 + \frac{1}{2}\kappa_{y,0}^2\sigma_y^2\\
&- \frac{K_{\mathrm{sc}}}{2}\ln(X+Y)\\
&+ \frac{\varepsilon_{\mathrm{dx}}^2}{2\sigma_x^2} + \frac{\varepsilon_{\mathrm{dy}}^2}{2\sigma_y^2} - \frac{\sigma_{\mathrm{p}}D_\delta}{\rho}.
\end{aligned} \tag{26}$$

Here, $X=\sqrt{\sigma_x^2+D_\delta^2}$ is the total RMS horizontal beam size, where σ_x is the betatron beam size, and D_δ is the "dispersion beam size," defined as $D_\delta \equiv D_x\sigma_{\rm p}$. $D_{{\rm p}\delta}$ is the derivative of D_δ, with $D_{{\rm p}\delta}\equiv {\rm d}D_\delta/{\rm d}s$. $Y=\sigma_y$ is the RMS vertical beam size because the dispersion effect is considered here only on x. The subscript "d" denotes the case with dispersion. A matched equation set with dispersion is

$$\begin{aligned}
&\kappa_{x,0}^2\sigma_{x,{\rm m}}-\frac{K_{\rm sc}}{2X_{\rm m}(X_{\rm m}+Y_{\rm m})}\sigma_{x,{\rm m}}-\frac{\varepsilon_{\rm dx}^2}{\sigma_x^3}=0,\\
&\kappa_{y,0}^2\sigma_{y,{\rm m}}-\frac{K_{\rm sc}}{2Y_{\rm m}(X_{\rm m}+Y_{\rm m})}\sigma_{y,{\rm m}}-\frac{\varepsilon_{\rm dy}^2}{\sigma_y^3}=0,\\
&\kappa_{x,0}^2D_{\delta,{\rm m}}-\frac{K_{\rm sc}}{2X_{\rm m}(X_{\rm m}+Y_{\rm m})}D_{\delta,{\rm m}}=\frac{\sigma_{\rm p}}{\rho},
\end{aligned}\tag{27}$$

where $X_{\rm m}$, $Y_{\rm m}$, and $D_{\delta,{\rm m}}$ are the matched solutions.

Based on the dimensionless parameters defined in Eq. (4), the Hamiltonian in Eq. (25) can be rewritten as

$$\begin{aligned}
\hat{H}_{\rm d,env}=&\frac{1}{2}(\hat{\sigma}_{\rm px}^2+\hat{\sigma}_{\rm py}^2+\hat{D}_{\rm p\delta}^2)+\frac{1}{2}(\hat{\sigma}_x^2+\eta^2\hat{\sigma}_y^2+\hat{D}_\delta^2)\\
&-\frac{\mu_{x,{\rm d}}(1+{\rm R})}{\sin\theta^2}\ln(\hat{X}+\hat{Y})+\frac{1-\mu_{x,{\rm d}}}{2}\frac{1}{\hat{\sigma}_x^2}\\
&+\frac{\varepsilon_{r,{\rm d}}^2(1-\mu_{x,{\rm d}})}{2}\frac{1}{\hat{\sigma}_y^2}+(1-\mu_{x,{\rm d}})\frac{\cos\theta}{\sin\theta}\hat{D}_\delta,
\end{aligned}\tag{28}$$

where $\hat{\sigma}_x$ and $\hat{\sigma}_y$ are the normalized betatron beam sizes, and η is the focusing ratio defined in Eq. (5). The dimensionless variables related to the dispersion in Eq. (28) are defined as

$$\begin{cases}
\hat{X} &= X/\sigma_{x,{\rm m}}\\
\hat{Y} &= Y/\sigma_{x,{\rm m}}\\
\hat{D}_\delta &= D_\delta/\sigma_{x,{\rm m}}\\
R &= Y_{\rm m}/X_{\rm m}\\
\sin\theta &= \sigma_{x,{\rm m}}/X_{\rm m}\\
\cos\theta &= D_{\delta,{\rm m}}/X_{\rm m}
\end{cases}\tag{29}$$

and

$$\begin{cases}
\varepsilon_{r,{\rm d}} &= \varepsilon_{\rm dy}/\varepsilon_{\rm dx}\\
\mu_{x,{\rm d}} &= \Delta\kappa_{x,d}^2/\kappa_{x,0}^2.
\end{cases}\tag{30}$$

Here, $\sin\theta=\sigma_{x,{\rm m}}/X_{\rm m}$ is the betatron ratio, and $\cos\theta=D_{\delta,{\rm m}}/X_{\rm m}$ is the dispersion ratio. $\Delta\kappa_{x,{\rm d}}^2=K_{\rm sc}/[2X_{\rm m}(X_{\rm m}+\sigma_{y,{\rm m}})]$ represents the space charge tune depression in the presence of dispersion.

We further introduce the "dispersion strength" $\Lambda\equiv D_{\delta,{\rm m}}^{(0)}/\sigma_{x,{\rm m}}^{(0)}$ to characterize the ratio of dispersion motion to betatron motion in zero-current beam case. Here, the superscript "(0)" denotes the absence of space charge, and $\sigma_{x,{\rm m}}=\sigma_{x,{\rm m}}^{(0)}/\sqrt[4]{1-\mu_x}$ and $D_{\delta,{\rm m}}=D_{\delta,{\rm m}}^{(0)}/(1-\mu_x)$. For typical synchrotrons such as the CSNS RCS [52, 53], the energy spread is frequently less than 1%, and we obtain $0<\Lambda<1.0$.

The dimensionless form of the dispersion-modified envelope equation set can be obtained from the Hamiltonian in Eq. (28) as follows:

$$\begin{aligned}
&\frac{{\rm d}^2}{{\rm d}\tau^2}\hat{\sigma}_x+\hat{\sigma}_x-\frac{\mu_{x,{\rm d}}(1+R)\hat{\sigma}_x}{\hat{X}(\hat{X}+\hat{Y})\sin\theta^2}-\frac{1-\mu_{x,{\rm d}}}{\hat{\sigma}_x^3}=0,\\
&\frac{{\rm d}^2}{{\rm d}\tau^2}\hat{\sigma}_y+\eta^2\hat{\sigma}_y-\frac{\mu_{x,{\rm d}}(1+{\rm R})\hat{\sigma}_{\rm y}}{\hat{Y}(\hat{X}+\hat{Y})\sin\theta^2}-\frac{\varepsilon_{r,{\rm d}}^2(1-\mu_{x,{\rm d}})}{\hat{\sigma}_y^3}=0,\\
&\frac{{\rm d}^2}{{\rm d}\tau^2}\hat{D}_\delta+\hat{D}_\delta-\frac{\mu_{x,{\rm d}}(1+R)\hat{D}_\delta}{\hat{X}(\hat{X}+\hat{Y})\sin\theta^2}-(1-\mu_{x,{\rm d}})\frac{\cos\theta}{\sin\theta}=0.
\end{aligned}\tag{31}$$

From Eq. (31), we obtain the matched beam sizes $\hat{\sigma}_{x,{\rm m}}=1$, $\hat{\sigma}_{y,{\rm m}}=r$, $\hat{D}_{\delta,{\rm m}}=\cot\theta$, and $\hat{X}_{\rm m}=\csc\theta$. Substituting the mismatch perturbations

$$\begin{aligned}
\hat{\sigma}_x&=1+\xi\\
\hat{\sigma}_y&=r+\zeta\\
\hat{D}_\delta&=\cot\theta+d
\end{aligned}\tag{32}$$

into the dispersion-modified envelope set of Eq. (31) ("d" is the perturbation on the dispersion), we obtain (more details in AppendixB)

$$\frac{{\rm d}^2}{{\rm d}\tau^2}\begin{pmatrix}\xi\\ \zeta\\ d\end{pmatrix}=-\begin{pmatrix}b_0 & b_1 & b_2\\ b_1 & b_3 & b_4\\ b_2 & b_4 & b_5\end{pmatrix}\begin{pmatrix}\xi\\ \zeta\\ d\end{pmatrix}\tag{33}$$

with the coefficients

$$\begin{aligned}
b_0&=4(1-\mu_{x,{\rm d}})+\frac{R+2}{R+1}\mu_{x,{\rm d}}\sin\theta^2,\\
b_1&=\frac{1}{R+1}\mu_{x,{\rm d}}\sin\theta,\\
b_2&=\frac{R+2}{R+1}\mu_{x,{\rm d}}\sin\theta\cos\theta,\\
b_3&=4(\eta^2-\frac{\mu_{x,{\rm d}}}{R})+\frac{2R+1}{R+1}\frac{\mu_{x,{\rm d}}}{R},\\
b_4&=\frac{1}{R+1}\mu_{x,{\rm d}}\cos\theta,\\
b_5&=(1-\mu_{x,{\rm d}})+\frac{R+2}{R+1}\mu_{x,{\rm d}}\cos\theta^2.
\end{aligned}\tag{34}$$

The coefficients in Eq. (34) can be expressed as a real symmetric matrix $B=\{b_{ij}\}$. Similar to the treatment described in Sect. 2, we obtain $B=U_{\rm d}\cdot{\rm diag}\{k_{\rm b}^2,k_{\rm q}^2,k_{\rm d}^2\}\cdot U_{\rm d}^T$. Compared with Eq. (10), the dispersion mode $k_{\rm d}$ can be identified [2]. The general solution to Eq. (33) takes the form

$$\begin{aligned}
\xi&=D_{11}\cos(k_{\rm b}\tau)+D_{12}\cos(k_{\rm q}\tau)+D_{13}\cos(k_{\rm d}\tau),\\
\zeta&=D_{21}\cos(k_{\rm b}\tau)+D_{22}\cos(k_{\rm q}\tau)+D_{23}\cos(k_{\rm d}\tau),\\
d&=D_{31}\cos(k_{\rm b}\tau)+D_{32}\cos(k_{\rm q}\tau)+D_{33}\cos(k_{\rm d}\tau).
\end{aligned}\tag{35}$$

Here, $D_{ij} = \sum_{k=1}^{3} U_{\mathrm{d},ij} U_{\mathrm{d},jk}^{T} \alpha_k$, with $\alpha_1 = \xi(0), \alpha_2 = \zeta(0), \alpha_3 = d(0)$.

However, in the presence of space charge and dispersion, the motion of a single particle is governed by

$$\frac{\mathrm{d}^2\hat{x}_\mathrm{d}}{\mathrm{d}\tau^2} + \hat{x}_\mathrm{d} = \frac{\mu_{\mathrm{d},x}(1+R)}{\sin\theta^2}\frac{\hat{x}_\mathrm{d}}{\hat{X}(\hat{X}+\hat{Y})} + \frac{\hat{\delta}}{2}(1-\mu_{\mathrm{d},x})\cos\theta \tag{36}$$

when the particle is inside the beam core ($|\hat{x}_\mathrm{d}| < \hat{X}\sin\theta$) and

$$\frac{\mathrm{d}^2\hat{x}_\mathrm{d}}{\mathrm{d}\tau^2} + \hat{x}_\mathrm{d} = \frac{\mu_{\mathrm{d},x}(1+R)\hat{x}_\mathrm{d}}{\hat{x}_\mathrm{d}^2 + |\hat{x}_\mathrm{d}|\sqrt{\hat{x}_\mathrm{d}^2 + (\hat{Y}^2-\hat{X}^2)\sin\theta^2}} + \frac{\hat{\delta}}{2}(1-\mu_{\mathrm{d},x})\cos\theta \tag{37}$$

when the particle is outside the beam core ($|\hat{x}_\mathrm{d}| > \hat{X}\sin\theta$). Here, $\hat{x}_\mathrm{d} = x/(2X_\mathrm{m})$ and $\hat{\delta} = \delta/\sigma_\mathrm{p}$ denote the ratio of the momentum spread between the single particle and beam core. Clearly, for $\sigma_\mathrm{p} = 0$, $\Lambda = 0$ and $\sin\theta = 1$, $R = r$. In this case, Eqs.(36) and (37) are equivalent to Eqs.(16) and (17).

An interesting question may be raised: Can the dispersion mode excite the 2:1 parametric resonance and induce a beam halo, as in the case of the two envelope modes discussed in Sec. 3? To analyze this problem, we plot the (half) wavenumber of the dispersion mode and the two envelope modes in Fig. 6, where the corresponding parameters are $\Lambda = 0.2, \eta = 1.0, R = 0.978$, and $\Lambda = 1.0, \eta = 1.0, R = 0.688$. Figure 6 shows that the half wavenumber of the dispersion mode is always below the lower limit of the test particle, indicating that the dispersion mode cannot induce a 2:1 resonance. Moreover, by inspecting the figure, we observe $k_{\mathrm{p,min}} < k_\mathrm{d} < k_{\mathrm{p,max}}$, implying the dispersion mode can generate a "1:1" parametric resonance on single particles.

In the following, we first demonstrate the mechanism of the 1:1 parametric resonance under the combined effect of dispersion and space charge and then show the damping effect on the beam halo formation owing to the moving stably fixed point (SFP) of single particles.

4.2 Dispersion-induced 1:1 parametric resonance

First, we consider the case of pure modes, in which only one of the breathing, quadrupole, or dispersion modes exists in the beam-core oscillation pattern. This can be achieved by setting the coefficients $D_{ij} = 0$ in Eq. (35).

The parametric resonances for the beam halo formation in the presence of space charge and dispersion can be analyzed using the dispersion-modified PCM in Eqs. (31), (36), and (37). As shown in Fig. (7), two resonant islands are

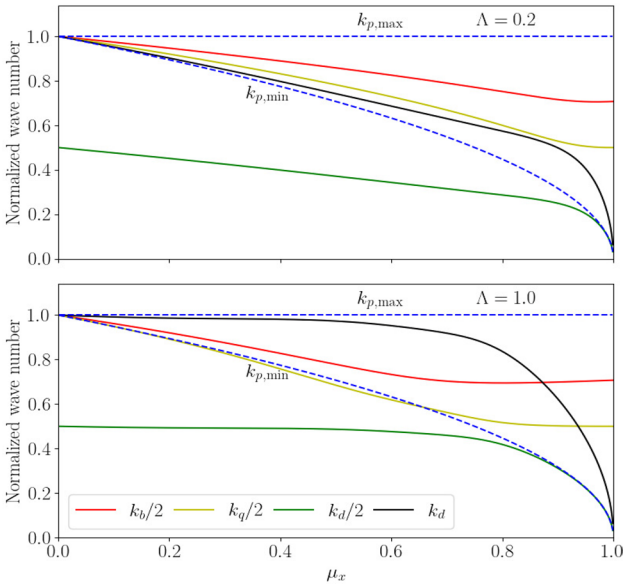

Fig. 6 (Color online) Half wavenumber of the breathing mode $k_\mathrm{b}/2$ (in red), quadrupole mode $k_\mathrm{q}/2$ (yellow), dispersion mode $k_\mathrm{d}/2$ (green), and wavenumber of the dispersion mode k_d (black) versus beam current in the unit of μ_x in the presence of dispersion with $\Lambda = 0.2$ (upper) and $\Lambda = 1.0$ (lower). The maximum ($k_{\mathrm{p,max}}$) and minimum ($\sum_a^b k_{\mathrm{p,min}}$) wavenumbers of single particles are also plotted for comparison

observed in panels (a) and (b), indicating the occurrence of a 2:1 resonance driven by the (pure) breathing and (pure) quadrupole modes. In the presence of the dispersion mode, a "crescent moon" island is observed, as shown in panel (c). Compared with the resonant islands in panels (a) and (b), only one island exists in panel (c), which is identified as the 1:1 resonance induced by the dispersion mode.

To better illustrate the 1:1 resonance, we plot the Poincaré section and normalized wavenumber of single particles in Fig. 8 (i.e., enlarged plot in Fig. 7c). We observe that in the "crescent moon" island, the wavenumber of single particle is locked and equal to wavenumber of the dispersion mode (marked as the yellow shaded area in Fig. 8b). This is a clear proof to support the "crescent moon" island in the Poincaré section is a 1:1 parametric resonance driven by the dispersion mode.

Next, we analyze the mixed mode, in which the breathing, quadrupole, and dispersion modes exist simultaneously. As shown in Fig. 7d, driven by the mixed modes, the 2:1 resonance driven by the two envelope modes and the 1:1 resonance induced by the dispersion mode exist. Furthermore, chaos is observed around the resonant islands. Panel (e) presents the corresponding wavenumbers of the three modes. Similar to the results shown in Fig. 4 in Sect. 3, the locking of the wavenumbers indicates the 2:1 and 1:1 parametric

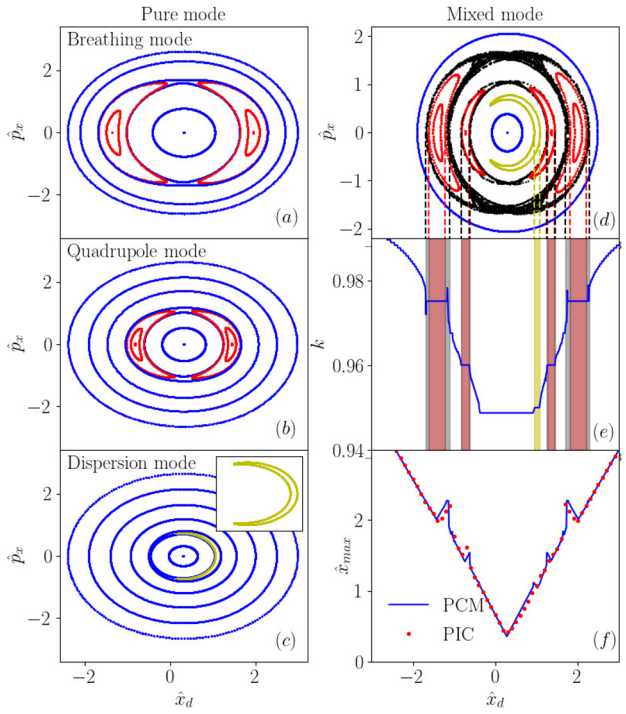

Fig. 7 (Color online) Poincaré sections of single particles with $\hat{\delta} = 3.0$ affected by the breathing mode **a**, quadrupole mode **b**, dispersion mode **c**, and mixed modes **d**, with $\Lambda = 0.2$ and $\mu_x = 0.1$. The wavenumbers of single particles for mixed modes as functions of initial positions are shown in **e**; the maximum displacement of single particle as a function of initial displacement is shown in **f**, compared with the simulation results (red dotted lines)

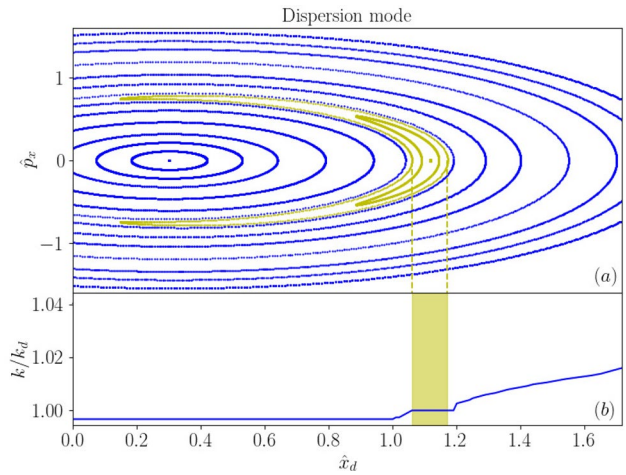

Fig. 8 (Color online) Poincaré section of single particles with $\hat{\delta} = 3.0$ affected by the dispersion mode **a** with $\Lambda = 0.2$ and $\mu_x = 0.1$; the wavenumber (normalized to the dispersion mode) of single particles as a function of initial positions is shown in **b**

resonances, which agrees with the resonant islands in panel (d). When chaos occurs, the wavenumber becomes random.

Table 2 Main parameters used in the simulation

Parameters	$\Lambda = 0.2$ case	$\Lambda = 1.0$ case
Length per cell (m)	14.2	14.2
Phase advance in x (deg)	108	108
Phase advance in y (deg)	108	108
Bending radius (m)	36.3	36.3
RMS momen. spread (%)	0.192	0.96
RMS emit. in x (mm·mrad)	30	30
RMS emit. in y (mm·mrad)	30	30
Intensity (particle numbers)	1.22×10^{10} ($\mu_x = 0.1$)	2.17×10^{10} ($\mu_x = 0.1$)

PIC simulations were conducted using the parameters of the $\Lambda = 0.2$ case, as shown in Table 2. The simulation results are shown in Fig. 7f. The simulation results of maximum displacements were in good agreement with the numerical calculations using the generalized PCM with dispersion.

4.3 Alleviation of the beam halo using strong dispersion

4.3.1 Motion of single particles with zero momentum deviation

We assume single particles with zero momentum deviation for the synchronous particles ($\hat{\delta} = 0$) in high-intensity synchrotrons. As shown in Fig. 6, for a large dispersion ($\Lambda = 1.0$), $k_q/2 < k_{p,min}$ holds when $\mu_x < 0.66$, indicating that the quadrupole mode cannot excite the 2:1 resonance in this region. In comparison, for the breathing mode, we obtain $k_b/2 > k_{p,min}$ and thus can trigger the 2:1 resonance.

The Poincaré sections of single particles with $\hat{\delta} = 0$ for the pure mode case with different dispersion strengths are shown in Fig. 9. Figure 9a and d shows that the areas of the 2:1 resonance islands driven by the breathing mode decrease with increasing dispersion strength. A similar phenomenon is observed in Fig. 9b and e: With an enhanced dispersion strength $\Lambda = 1.0$, the 2:1 resonance driven by the quadrupole mode disappears. We attribute this result to the fact that the dispersion effect can reduce the 2:1 resonance. Second, no resonance islands are observed in Fig. 9c and f, implying that the dispersion mode cannot induce a 2:1 resonance, which agrees with the analysis from Fig. 6.

The Poincaré sections for the mixed mode case are shown in Fig. 10. The chaos existed around the resonance islands driven by mixed modes. Compared with Fig. 10a, we observe the chaos in Fig. 10d weakens as the dispersion

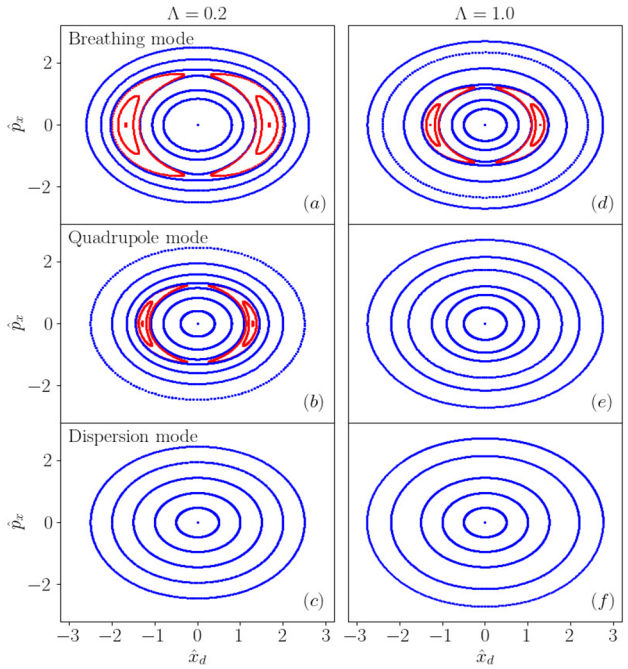

Fig. 9 (Color online) Poincaré section of single particles with $\hat{\delta} = 0.0$ affected by the breathing mode **a** and **d**, the quadrupole mode **b** and **e**, and the dispersion mode **c** and **f**, with $\Lambda = 0.2$ (left column) and $\Lambda = 1.0$ (right column) under the fixed space charge strength $\mu_x = 0.1$

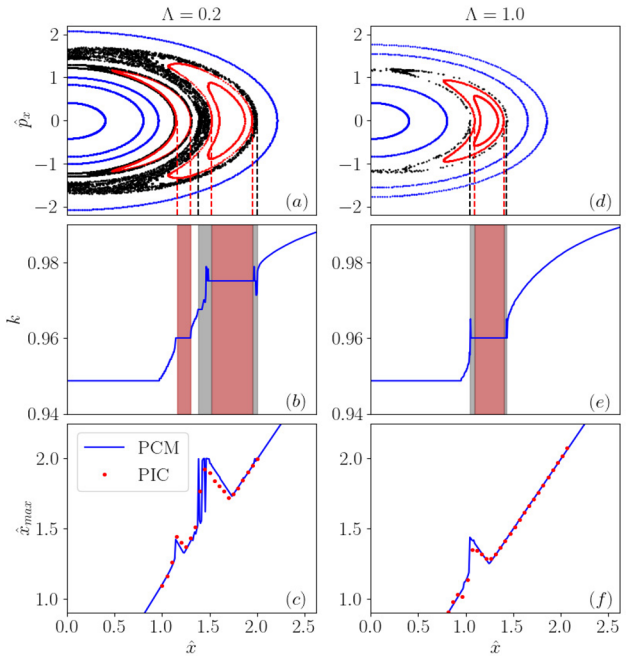

Fig. 10 (Color online) Motion of zero-momentum-deviation single particles ($\hat{\delta} = 0.0$) with different initial positions in the presence of mixed mode with moderate ($\Lambda = 0.2$, left column **a**, **b** and **c**) and strong dispersion ($\Lambda = 1.0$, right column **d**, **e** and **f**) under the fixed space charge tune depression $\mu_x = 0.1$. The Poincaré sections are shown in **a** and **d**; the wavenumber of single particle as a function of initial positions is shown in **b** and **e**; and the maximum displacement of single particle as a function of initial displacement is shown in **c** and **f**, compared with the simulation results (red dotted lines)

strength increases ($\Lambda = 1.0$). The wavenumbers of single particles with different initial positions are shown in in Fig. 10b and e, where the red and gray shadows represent the resonance and chaos, respectively. PIC simulations were performed for $\Lambda = 0.2$ and $\Lambda = 1.0$ using the parameters listed in Table 2. The simulation results for the maximum displacements are shown in Fig. 10c and f. The simulation results were in good agreement with the PCM calculations.

4.3.2 Motion of single particles with large momentum deviation

For the single particles with large momentum deviation, the SFP can "move" out of the beam core in the presence of the dispersion effect. As an example, we plot four SFPs with different momentum deviations in phase space in the panel (a) of Fig. 11. We set $\Lambda = 1.0$ for the beam core. We observe that with $\hat{\delta} = 3.0$ and 4.0 (marked as S_3 and S_4), the two SFPs are located outside the beam core.

For a more illustrative discussion, the scanning of the maximum excursion of an edge particle is shown in Fig. 12. The scan is performed by varying the dispersion strength of the beam core Λ and the momentum deviation ratio of

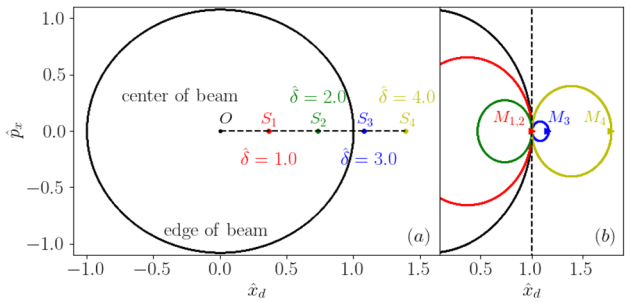

Fig. 11 (Color online) **a** Example with $\Lambda = 1.0, \mu_x = 0.1$ of the moving SFP at four different positions (inside the beam core S_1, S_2, and outside the beam core S_3, S_4) with increasing momentum deviations of single particles ($\hat{\delta} = 1.0, 2.0, 3.0, 4.0$); **b** example with $\Lambda = 1.0, \mu_x = 0.1$ of four single particles with their initial positions at the edge of the beam core and different momentum deviations $\hat{\delta} = 1.0, 2.0, 3.0, 4.0$. The trajectories of the two particles inside the beam core (in red and green), with their maximum displacements M_1 and M_2 overlapping. The trajectories of the other two particles outside the beam core (in yellow and blue), with their maximum displacements M_3 and M_4

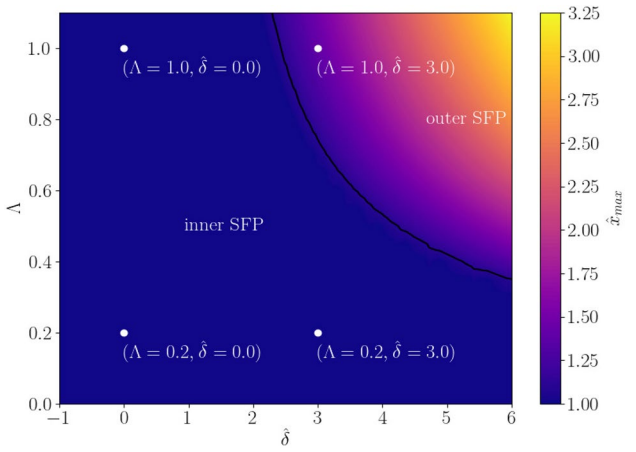

Fig. 12 (Color online) Scan of the maximum motion of the "edge particles" ($\hat{x}_{\max}$) with varying momentum deviations ($\hat{\delta}$) and dispersion strength (Λ), under the fixed space charge tune depression $\mu_x = 0.1$. Black line denotes the boundary between the area of inner SFPs ($x_{\max} = 1$), and the area of outer SFPs ($x_{\max} > 1$)

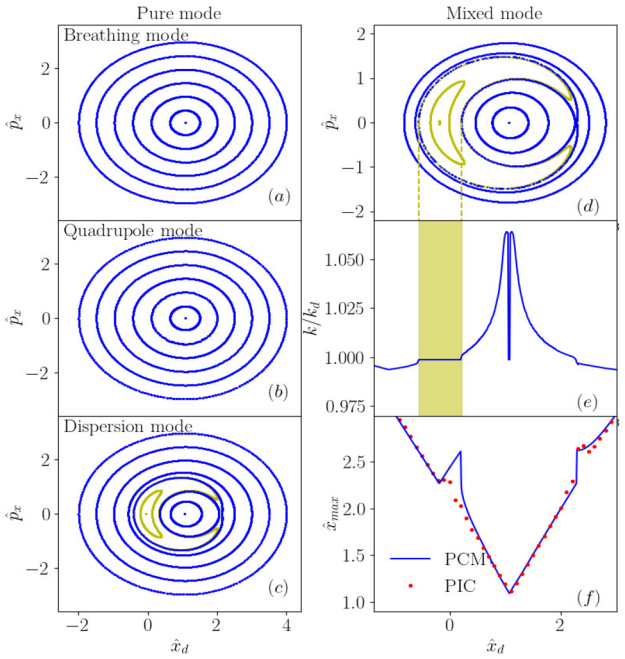

Fig. 13 (Color online) Poincaré sections of single particles with $\hat{\delta} = 3.0$ affected by the breathing mode **a**, quadrupole mode **b**, dispersion mode **c** and mixed modes **d**, respectively, with $\Lambda = 1.0$ and $\mu_x = 0.1$. The wavenumbers (normalized to the dispersion mode) of single particles for mixed modes as a function of initial positions are shown in **e**; the maximum displacement of single particle as a function of initial displacement is shown in **f**, compared with the simulation results (red dotted lines)

the single particle $\hat{\delta}$. Here, the edge particles are defined that their initial positions are set to "sit" on the edge of the beam core, i.e., $\hat{x}_{\rm d}(0) = 1$. For different $\hat{\delta}$ and Λ values, the edge particles have different maximum excursions, $\hat{x}_{\max}$. The advantage of using edge particles is that, (shown in Fig. 11b), for the edge particles with $\hat{x}_{\max} = 1$, the SFPs are located inside the beam core, shown as the region "inner SFP" in Fig. 12; for the edge particles with $\hat{x}_{\max} > 1$, shown as the region "outer SFP" in Fig. 12.

Figure 12 shows that, for single particles with SFPs inside the beam core, the condition $k_{\rm p,min} = \sqrt{1-\mu_x}$ is always satisfied. For SFPs outside the beam core ($\hat{x}_{\max} > 1$), we obtain $k_{\rm p,min} > \sqrt{1-\mu_x}$. For a sufficiently large $\hat{\delta}$, $k_{\rm p,min} > k_{\rm b}/2$. In this case, the 2:1 resonance cannot be driven by the breathing mode. In other words, the large off-momentum deviations of a single particle can dampen the 2:1 resonance. To show this more clearly, the motions of single particles with $\hat{\delta} = 3.0$, affected by the breathing, quadruple, and dispersion modes are shown in Fig. 13a–c, respectively. The 2:1 resonances driven by the breathing and quadrupole modes are dampened because of the large momentum deviation $\hat{\delta}$, and only the 1:1 resonance driven by the dispersion mode can be observed. Panel (d) shows the mixed case. Only the 1:1 resonance caused by the dispersion mode exists. The locking of the wavenumber is presented in panel (e), where the condition $k = k_{\rm d}$ is satisfied, indicating that the 1:1 resonance is a parametric resonance.

PIC simulations were conducted using the parameters listed for $\Lambda = 1.0$, as shown in Table 2, and the simulation results are shown in Fig. 13f. The simulation results of the maximum displacements agreed closely with the numerical calculations based on the dispersion-modified PCM.

5 High-order mode in large mismatch oscillations

The analysis of the beam halo formation in the preceding sections is based on perturbation theory, where single-particle oscillations with small amplitudes are considered and high-order terms are neglected. In this section, we investigate single-particle motion driven by the mismatch oscillation of the beam core with a large amplitude, in which high-order oscillation modes are considered. An interesting question is whether these high-order oscillation modes can induce a beam halo. Note that high-order modes in the large mismatch discussed here should be distinguished from the high-order resonances of the low-order modes. For example, the 8:3 resonance shown in Fig. 2 is an eighth-order resonance driven by low-order (breathing) modes.

For simplicity, we consider a round beam traveling in a symmetrical focusing channel. In this case, the envelope equation for the beam core (Eq. (7)) can be expressed as

$$\frac{\mathrm{d}^2\hat{\sigma}}{\mathrm{d}\tau^2} + \hat{\sigma} - \frac{\mu}{\hat{\sigma}} - \frac{1-\mu}{\hat{\sigma}^3} = 0. \tag{38}$$

The solution to Eq. (38) can be expressed as a triangular series:

$$\hat{\sigma} = 1 + a_1 \cos 2\Omega\tau + a_2 \cos 4\Omega\tau + \ldots + a_n \cos 2n\Omega\tau, \tag{39}$$

where 2Ω represents the wavenumber of the breathing mode (here, we use 2Ω to replace k_b for convenience of derivation), and $2n\Omega$ ($n > 1$) denotes the wavenumbers of the high-order modes.

However, the equations of motion for single particles in Eqs. (16) and (17) can be approximated using a cubic term [26]:

$$\frac{\mathrm{d}^2\hat{x}}{\mathrm{d}\tau^2} + \hat{x} - \mu\left(\frac{\hat{x}}{\hat{\sigma}^2} - \frac{\hat{x}^3}{4}\right) = 0. \tag{40}$$

Substituting Eq. (39) into Eq. (40), we obtain the Hamiltonian of a single particle with large mismatch oscillations in the beam core:

$$H_\mathrm{L} = \frac{\hat{p}_x^2}{2} + \frac{\omega^2\hat{x}^2}{2}\left(1 + \sum\nolimits_{i=1}^{n} h_i \cos 2i\Omega\tau\right) + \alpha\frac{\hat{x}^4}{4}, \tag{41}$$

with the parameters $\omega^2 = 1-\mu$, $h_i = -2\mu a_i/(1-\mu)$ and $\alpha = \mu/4$. Using the generating function,

$$F_2(\hat{x}, P, \tau) = \frac{\hat{x}P}{\cos\Omega\tau} - \left(\frac{P^2}{2\omega} + \omega\frac{\hat{x}^2}{2}\right)\tan\Omega\tau, \tag{42}$$

We can convert the Hamiltonian in Eq. (41) into

$$\hat{H}_\mathrm{L} = \hat{H}_{\mathrm{L},0} + \hat{H}_{\mathrm{L},1} + \ldots + \hat{H}_{\mathrm{L},n}, \tag{43}$$

where $\hat{H}_{\mathrm{L},0}$ and $\hat{H}_{\mathrm{L},n}$ ($n > 0$) represent the Hamiltonians of the single-particle motion for the lowest-order (breathing) and high-order modes, respectively. The average Hamiltonian $\hat{H}_{\mathrm{L},n}$ over a mismatched oscillation period $T = 2\pi/\Omega$ is

$$\langle\hat{H}_{\mathrm{L},n}\rangle = 0 \ (n > 0) \tag{44}$$

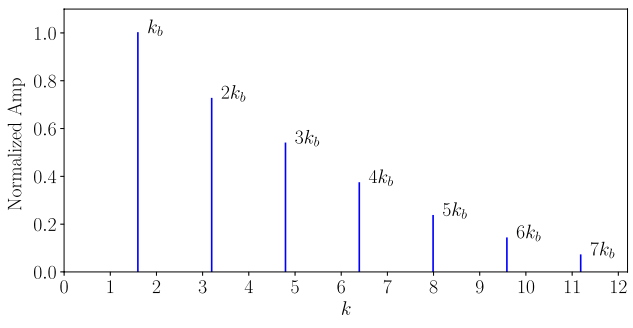

Fig. 14 (Color online) Frequency spectrum of the beam envelope oscillations with large mismatch

which indicates that the contribution of the higher-order modes over one oscillation period to the 2:1 resonance is zero (more details are given in Appendix C). Consequently, higher-order modes cannot excite the 2:1 resonance.

For example, we numerically solve Eq. (38) with the initial condition $\hat{\sigma}(0) = 0.6$ (i.e., 40% mismatch). The numerical results of the beam envelope oscillation is analyzed using FFT, and the frequency (wavenumber) spectrum is shown in Fig. 14. High-order modes (up to sixth order) are observed, which are caused by a large mismatch (40%). The wavenumber (frequency) of the higher modes (nk_b) is a multiple of the fundamental mode (k_b). The amplitudes of the modes decreased with increasing mode order.

The Poincaré section and corresponding wavenumbers of single particles with different initial positions under 40% mismatch are calculated using Eqs. (38) and (40), as shown in Fig. 15a and b, respectively. Within the 2:1 resonance islands, we obtain $k = k_\mathrm{b}/2$, indicating it is driven by the lowest-order (breathing) mode. No 2:1 resonances driven by higher-order modes are observed, which agrees with the analysis based on the Hamiltonian in Eq. (44).

A PIC simulation was conducted based on the parameters of the "round beam" shown in Table 1. In the simulation, an initial KV distribution of 200,000 macroparticles

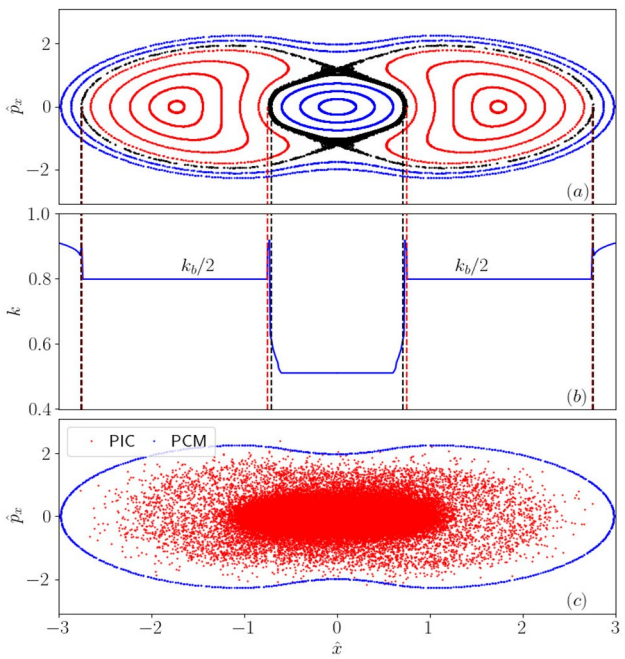

Fig. 15 (Color online) Motion of single particles with different initial positions in the presence of large mismatch with strong space charge tune depression $\mu_x = 0.8$. The Poincaré sections are shown in **a**; the wavenumber of single particle as a function of initial positions is shown in **b**; and the contour of the Poincaré section is shown in **c**, compared with the simulation results (red dotted lines)

was tracked for 500 turns, and the results are shown in Fig. 15c. A "peanut" shape of the halo particle distribution was observed in the simulation result, agreeing with the contour of the Poincaré section, which was numerically calculated using Eqs. (16), (17), and (38).

Based on closer observation in Fig. 15a, we observe the chaotic regions exist around the resonance islands (black). The physical mechanism of chaos formation can be analyzed as follows. To clarify the flow of the following text, we distinguish two types of particle-core resonances:

1. Low-order particle-core resonances driven by high-order beam oscillation modes (be proved not existing in Eq. (44));
2. High-order particle-core resonances driven by low-order beam oscillation modes.

In the former case, high-order modes cannot induce low-order resonances, as discussed using Eq. (44). To analyze the latter case, we use a perturbation method with a large mismatch of 40% ($\xi(0) = \zeta(0) = 0.4$ in Eq. (10)) to maintain only the breathing mode in the system and neglect higher-order modes because they do not contribute to the resonances. Thus, it is convenient to plot the Poincaré section, as shown in Fig. 16. Figure 16a and b shows that several high-order resonance islands exist: the 3:1 resonance (yellow), 4:1 resonance (orange), skew 4:1 resonance (brown), 7:2 resonance (green), and 8:3 resonance (purple). The lock of the wavenumber of the modes for high-order resonance was calculated and is shown in panel (c) of Fig. 16.

A detailed observation in Fig. 16 shows that the chaos region can be divided into inner and outer regions. The "outer chaos" is caused by the mixture of the 2:1 resonance and the higher-order resonance, such as the 3:1 (yellow) and 8:3 (purple) resonances. In comparison, the "inner chaos" is closer to the beam core and much weaker. We attribute it to the fact that the inner chaos is caused by the mixture of high-order resonances, the 4:1 and the "skew" 4:1 as shown in Fig. 16. The outer chaos is driven by the lowest-order (2:1) resonances and is thus much stronger.

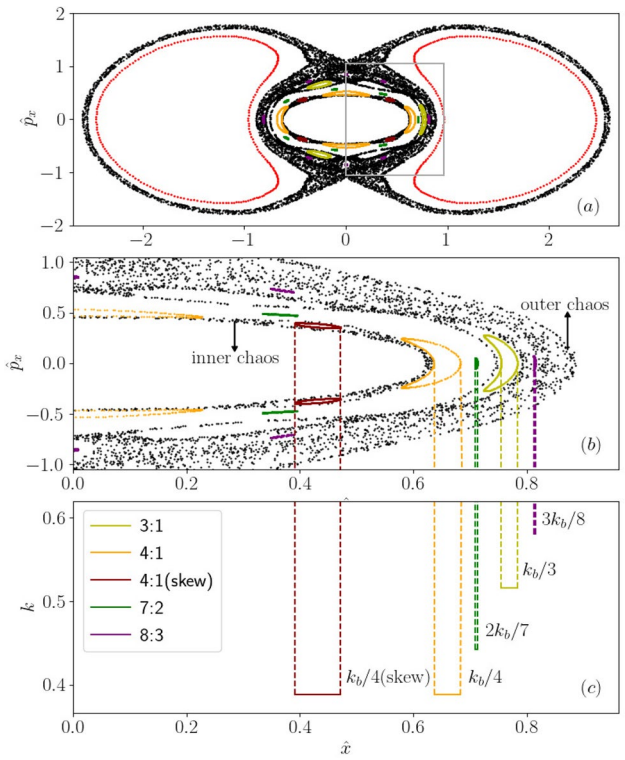

Fig. 16 (Color online) Motion of single particles with different initial positions under the breathing mode with a strong space charge tune depression $\mu_x = 0.8$. The Poincaré sections are shown in **a**; the enlarged plot of **a** is shown in **b**, including the 3:1 resonance (yellow), the 4:1 resonance (orange), the skew 4:1 resonance (brown), the 7:2 resonance (green), and the 8:3 resonance (purple); and the wavenumbers of single particles as functions of initial positions are shown in (c)

6 Summary

We have analyzed beam halo formation driven by the parametric resonance between single particles and the beam core in high-intensity synchrotrons. In the absence of dispersion, we observe several high-order resonances in addition to the 2:1 resonance. Moreover, chaos exists with a mixture of parametric resonances and can be weakened by the asymmetry of elliptical beams. In the presence of the combined effect of space charge and dispersion, we find that the dispersion mode can drive the 1:1 parametric resonance and discussed its physical mechanism in detail. In addition, we demonstrated that the beam halo can be alleviated by a large dispersion. For large mismatch oscillations, we proved that higher-order modes exist; however, they are unable to drive 2:1 parametric resonance.

We expect that the 1:1 parametric resonance will have implications for the design and operation of high-intensity synchrotrons. Furthermore, the role of synchrotron motion in beam halo formation warrants further investigation.

Appednix A: Equations of motion for the envelope perturbation

For the Hamiltonian of the envelope with perturbations in Eq. (9) in Sect. 2,

$$\begin{aligned}\hat{H}_{\rm per} =& \frac{1}{2}\left[(\hat{\sigma}_{{\rm p}x,{\rm m}}+\xi_{\rm p})^2+(\hat{\sigma}_{{\rm p}y,{\rm m}}+\zeta_{\rm p})^2\right.\\ &\left.+(1+\xi)^2+\eta^2(r+\zeta)^2\right]\\ &-\mu_x(1+r)\ln(1+r+\xi+\zeta)\\ &+\frac{1-\mu_x}{2(1+\xi)^2}+\frac{\varepsilon_{\rm r}^2(1-\mu_x)}{2(r+\zeta)^2}.\end{aligned} \tag{A1}$$

The Hamiltonian's equation of motion is

$$\begin{aligned}\frac{{\rm d}\xi}{{\rm d}\tau}&=\frac{\partial\hat{H}}{\partial\xi_{\rm p}}\frac{{\rm d}\xi_{\rm p}}{{\rm d}\tau}=-\frac{\partial\hat{H}}{\partial\xi}\\ \frac{{\rm d}\zeta}{{\rm d}\tau}&=\frac{\partial\hat{H}}{\partial\zeta_{\rm p}}\frac{{\rm d}\zeta_{\rm p}}{{\rm d}\tau}=-\frac{\partial\hat{H}}{\partial\zeta}.\end{aligned} \tag{A2}$$

Here, $(\xi,\xi_{\rm p})$ and $(\zeta,\zeta_{\rm p})$ are pairs of dimensionless conjugate variables. After neglecting the higher-order items, we obtain from Eq. (A2)

$$\begin{aligned}\frac{{\rm d}^2\xi}{{\rm d}\tau^2}&=-\frac{\partial\hat{H}}{\partial\xi}\\ &=-\left[1+\xi-\frac{\mu_x}{1+(\xi+\zeta)/(1+r)}\right.\\ &\left.-(1-\mu_x)\frac{1}{(1+\xi)^3}\right]\\ &\approx-\left[4(1-\mu_x)+\frac{2+r}{1+r}\mu_x\right]\xi-\frac{\mu_x}{1+r}\zeta,\end{aligned} \tag{A3}$$

and

$$\begin{aligned}\frac{{\rm d}^2\zeta}{{\rm d}\tau^2}&=-\frac{\partial\hat{H}}{\partial\zeta}\\ &\approx-\left[4(\eta^2-\frac{\mu_x}{r})+\frac{1+2r}{r(1+r)}\mu_x\right]\zeta-\frac{\mu_x}{1+r}\xi\end{aligned} \tag{A4}$$

where we use the following relation:

$$\frac{\varepsilon_{\rm r}^2}{r^3}=\frac{r\eta^2-\mu_x}{1-\mu_x}. \tag{A5}$$

Equations (A3) and (A4) are the equations of motion for the envelope perturbations in Eq. (10) in Sect. 2.

Appendix B: Equations of motion for the envelope perturbation with dispersion

The Hamiltonian of the envelope with the dispersion in Eq. (28) in Sect. 4 is

$$\begin{aligned}\hat{H}_{\rm env} =& \frac{1}{2}(\hat{\sigma}_{{\rm p}x}^2+\hat{\sigma}_{\rm py}^2+\hat{D}_{{\rm p}\delta}^2)+\frac{1}{2}(\hat{\sigma}_x^2+\eta^2\hat{\sigma}_y^2+\hat{D}_\delta^2)\\ &-\frac{\mu_x(1+{\rm R})}{\sin\theta^2}\ln(\hat{X}+\hat{Y})\\ &+\frac{1-\mu_x}{2}\frac{1}{\hat{\sigma}_x^2}+\frac{\varepsilon_{\rm r}^2(1-\mu_x)}{2}\frac{1}{\hat{\sigma}_y^2}+(1-\mu_x)\frac{\cos\theta}{\sin\theta}\hat{D}_\delta\\ =& \frac{1}{2}(\hat{\sigma}_{{\rm p}x}^2+\hat{\sigma}_{\rm py}^2+\hat{D}_{{\rm p}\delta}^2)+V(\hat{\sigma}_x,\hat{\sigma}_y,\hat{D}_\delta).\end{aligned} \tag{B1}$$

We define the perturbative variables (here, the subscript 'd' in $\mu_{x,{\rm d}}$ and $\varepsilon_{r,{\rm d}}$ of Eq. (28) is neglected for simplicity) as follows:

$$\begin{aligned}\hat{\sigma}_x&=1+\xi\\ \hat{\sigma}_{{\rm p}x}&=\hat{\sigma}_{{\rm p}x,{\rm m}}+\xi_{\rm p}\\ \hat{\sigma}_y&=r+\zeta\\ \hat{\sigma}_{\rm py}&=\hat{\sigma}_{{\rm py},{\rm m}}+\zeta_{\rm p}\\ \hat{D}_\delta&=\cot\theta+d_\delta\\ \hat{D}_{{\rm p}\delta}&=\hat{D}_{{\rm p}\delta,{\rm m}}+d_{{\rm p}\delta}.\end{aligned} \tag{B2}$$

By substituting the perturbative variables in Eqs. (B2) into Eq. (B1), we obtain the Hamiltonian of the envelope with perturbations:

$$\hat{H}(\xi,\xi_{\rm p},\zeta,\zeta_{\rm p},d_\delta,d_{{\rm p}\delta})=P(\xi_{\rm p},\zeta_{\rm p},d_{{\rm p}\delta})+V(\xi,\zeta,d_\delta) \tag{B3}$$

which consists of the "kinetic energy" term

$$\begin{aligned}P(\xi_{\rm p},\zeta_{\rm p},d_{{\rm p}\delta})=&\frac{1}{2}[(\hat{\sigma}_{{\rm p}x,{\rm m}}+\xi_{\rm p})^2\\ &+(\hat{\sigma}_{{\rm py},{\rm m}}+\zeta_{\rm p})^2+(\hat{D}_{{\rm p}\delta,{\rm m}}+d_{{\rm p}\delta})^2],\end{aligned} \tag{B4}$$

and "potential" term

$$\begin{aligned}V(\xi,\zeta,d_\delta)=&\frac{1}{2}[(1+\xi)^2+(r+\zeta)^2+(\cot\theta+d_\delta)^2]\\ &-\frac{\mu_x(1+{\rm R})}{\sin\theta^2}\ln\left[\sqrt{(1+\xi)^2+(\cot\theta+d_\delta)^2}+r+\zeta\right]\\ &+\frac{1-\mu_x}{2}\frac{1}{(1+\xi)^2}+\frac{\varepsilon_{\rm r}^2(1-\mu_x)}{2}\frac{1}{(r+\zeta)^2}\\ &+(1-\mu_x)\frac{\cos\theta}{\sin\theta}(\cot\theta+d_\delta).\end{aligned} \tag{B5}$$

The equations of motion for envelope perturbations with dispersion can be expressed as

$$\frac{{\rm d}^2\xi}{{\rm d}\tau^2}=-\frac{\partial\hat{V}}{\partial\xi}\approx-(b_0\xi+b_1\zeta+b_2d_\delta) \tag{B6}$$

$$\frac{{\rm d}^2\zeta}{{\rm d}\tau^2}=-\frac{\partial\hat{V}}{\partial\zeta}\approx-(b_1\xi+b_3\zeta+b_4d_\delta) \tag{B7}$$

$$\frac{\mathrm{d}^2 d_\delta}{\mathrm{d}\tau^2} = -\frac{\partial \hat{V}}{\partial d_\delta} \approx -(b_2\xi + b_4\zeta + b_5 d_\delta) \tag{B8}$$

with the parameters

$$\begin{aligned} b_0 &= 4(1-\mu_x) + \frac{R+2}{R+1}\mu_x \sin\theta^2 \\ b_1 &= \frac{1}{R+1}\mu_x \sin\theta \\ b_2 &= \frac{R+2}{R+1}\mu_x \sin\theta\cos\theta \\ b_3 &= 4(\eta^2 - \frac{\mu_x}{R}) + \frac{2R+1}{R+1}\frac{\mu_x}{R} \\ b_4 &= \frac{1}{R+1}\mu_x \cos\theta \\ b_5 &= (1-\mu_x) + \frac{R+2}{R+1}\mu_x \cos\theta^2, \end{aligned} \tag{B9}$$

which is Eq. (33) in Sec. 4.

Appednix C: Calculation of the higher-order mode contributions

The Hamiltonian for the lowest- and higher-order modes in Eq. (43) is

$$\begin{aligned} \hat{H}_{\mathrm{L},0} = &\frac{1}{2}\left(1-\frac{\Omega}{\omega}\right)P^2 + \frac{\omega^2}{2}\left(1-\frac{\Omega}{\omega}\right)Q^2 \\ &- \frac{\omega^2 h_1}{2}\left(Q\cos\Omega\tau + \frac{P}{\omega}\sin\Omega\tau\right)^2\cos 2\Omega\tau \\ &+ \frac{\alpha}{4}\left(Q\cos\Omega\tau + \frac{P}{\omega}\sin\Omega\tau\right)^4 \end{aligned} \tag{C1}$$

$$\hat{H}_{\mathrm{L},n} = -\frac{\omega^2 h_{n+1}}{2}\left(Q\cos\Omega\tau + \frac{P}{\omega}\sin\Omega\tau\right)^2\cos 2(n+1)\Omega\tau \tag{C2}$$

For the Hamiltonian of the lowest-order mode $\hat{H}_{\mathrm{L},0}$, by taking the average over one perturbation oscillation period, we obtain

$$\begin{aligned} \langle\hat{H}_{\mathrm{L},0}\rangle = &\frac{1}{2}\left(1-\frac{\Omega}{\omega}\right)\hat{P}^2 + \frac{\omega^2}{2}\left(1-\frac{\Omega}{\omega}\right)\hat{Q}^2 \\ &- \frac{\omega^2 h_1}{2}\left(\hat{Q}\langle\cos\Omega\tau^2\cos 2\Omega\tau\rangle + \frac{\hat{P}}{\omega}\langle\sin\Omega\tau^2\cos 2\Omega\tau\rangle\right. \\ &\left.+ \frac{2\hat{P}\hat{Q}}{\omega}\langle\sin\Omega\tau\cos\Omega\tau\cos 2\Omega\tau\rangle\right) \\ &+ \frac{\alpha}{4}\left(\hat{Q}^4\langle\cos\Omega\tau^4\rangle + \frac{6\hat{Q}^2\hat{P}^2}{\omega^2}\langle\sin\Omega\tau^2\cos\Omega\tau^2\rangle\right. \\ &+ \frac{\hat{P}^4}{\omega^4}\langle\sin\Omega\tau^4\rangle + \frac{4\hat{Q}^3\hat{P}}{\omega}\langle\sin\Omega\tau\cos\Omega\tau^3\rangle \\ &\left.+ \frac{4\hat{Q}\hat{P}^3}{\omega^3}\langle\sin\Omega\tau^3\cos\Omega\tau\rangle\right), \end{aligned} \tag{C3}$$

where $\langle x(\tau)\rangle = (1/T)\int x(\tau)\mathrm{d}\tau$. Because we know that

$$\begin{aligned} &\langle\cos\Omega\tau^4\rangle = \langle\sin\Omega\tau^4\rangle = \frac{3}{8} \\ &\langle\sin\Omega\tau^2\cos\Omega\tau^2\rangle = \frac{1}{8} \\ &\langle\sin\Omega\tau^3\cos\Omega\tau\rangle = \langle\sin\Omega\tau\cos\Omega\tau^3\rangle = 0, \end{aligned} \tag{C4}$$

Eq. (C3) becomes

$$\begin{aligned} \langle\hat{H}_{\mathrm{L},0}\rangle = &\frac{\omega^2\hat{Q}^2}{2}\left(1-\frac{\Omega}{\omega}+\frac{h_1}{4}\right) + \frac{\hat{P}^2}{2}\left(1-\frac{\Omega}{\omega}-\frac{h_1}{4}\right) \\ &+ \frac{3}{32}\alpha\left(\hat{Q}^2 + \frac{\hat{P}^2}{\omega^2}\right)^2, \end{aligned} \tag{C5}$$

which agrees with Eq. (18). [26].

Next, for the Hamiltonian of the high-order modes $\hat{H}_{\mathrm{L},n}$ ($n > 0$), we have

$$\begin{aligned} \langle\hat{H}_{\mathrm{L},n}\rangle = -\frac{\omega^2 h_{n+1}}{2}&\left(\hat{Q}\langle\cos\Omega\tau^2\cos 2(n+1)\Omega\tau\rangle\right. \\ &+ \frac{2\hat{Q}\hat{P}}{\omega}\hat{Q}\langle\sin\Omega\tau\cos\Omega\tau\cos 2(n+1)\Omega\tau\rangle \\ &\left.+ \frac{\hat{P}}{\omega}\langle\sin\Omega\tau^2\cos 2(n+1)\Omega\tau\rangle\right). \end{aligned} \tag{C6}$$

By using the relation

$$\begin{aligned} &\langle\cos^2\Omega\tau\cos 2(n+1)\Omega\tau\rangle = 0 \\ &\langle\sin^2\Omega\tau\cos 2(n+1)\Omega\tau\rangle = 0 \\ &\langle\cos\Omega\tau\sin\Omega\tau\cos 2(n+1)\Omega\tau\rangle = 0, \end{aligned} \tag{C7}$$

we obtain $\langle\hat{H}_{\mathrm{L},n}\rangle = 0$, which indicates that during one oscillation period, the average interaction between single particles and the beam core via high-order oscillation modes is zero. Thus, the high-order modes are unable to excite the 2:1 parametric resonance.

Acknowledgements The authors would like to thank Kazuhito Ohmi for the valuable discussions and suggestions.

Author contributions All authors contributed to the study conception and design. Material preparation, data collection, and analysis were performed by Jia-Yin Du, Yao-Shuo Yuan, Morteza Aslaninejad, Jing-Tong Du, Ming-Yang Huang, and S. Wang. The first draft of the manuscript was written by Jia-Yin Du, and all authors commented on previous versions of the manuscript. All authors read and approved the final manuscript.

Data availability The data that support the findings of this study are openly available in Science Data Bank at https://cstr.cn/31253.11.sciencedb.j00186.00814 and https://doi.org/10.57760/sciencedb.j00186.00814

References

1. C. Chen, R.C. Davidson, Nonlinear resonances and chaotic behavior in a periodically focused intense charged-particle beam. Phys. Rev. Lett. **72**, 2195 (1994). https://doi.org/10.1103/PhysRevLett.72.2195
2. Y.S. Yuan, O. Boine-Frankenheim, G. Franchetti et al., Dispersion-induced beam instability in circular accelerators. Phys. Rev. Lett. **118**, 154801 (2017). https://doi.org/10.1103/PhysRevLett.118.154801
3. C. Li, Y.L. Zhao, Envelope instability and the fourth order resonance. Phys. Rev. ST Accel. Beams. **17**, 124202 (2014). https://doi.org/10.1103/PhysRevSTAB.17.124202
4. C. Chen, Q. Qian, R.C. Davidson, Chaotic behavior and halo development in the transverse dynamics of heavy-ion beams. Fusion Eng. Des. **32–33**, 159–167 (1996). https://doi.org/10.1016/S0920-3796(96)00464-4
5. C. Li, Z.C. Liu, Y.L. Zhao et al., Nonlinear resonance and envelope instability of intense beam in axial symmetric periodic channel. Nucl. Instrum. Meth. A **813**, 13–18 (2016). https://doi.org/10.1016/j.nima.2015.12.056
6. Z.H. Li, J.Y. Tang, F. Yan et al., Longitudinal instability caused by long drifts in the C-ADS injector-I. Chinese Phys. C **37**, 037005 (2013). https://doi.org/10.1088/1674-1137/37/3/037005
7. X.L. Lu, Y. Zhang, J.R. Wang et al., Transport characteristics of space charge dominated multi-species deuterium beam in electrostatic low energy beam line. Nucl. Sci. Tech. **29**(4), 51 (2018). https://doi.org/10.1007/s41365-018-0384-2
8. X.L. Lu, Z.E. Yao, Y. Zhang et al., Simulation of high-intense beam transport in electrostatic accelerating column. Nucl. Sci. Tech. **26**(6), 060201 (2015). https://doi.org/10.13538/j.1001-8042/nst.26.060201
9. Y. Yang, Z. Liu, W. Zhang et al., Simulation of a low energy beam transport line. Nucl. Sci. Tech. **23**(2), 83–89 (2012). https://doi.org/10.13538/j.1001-8042/nst.23.83-89
10. Y. Li, Y.S. Yuan, S.Y. Xu et al., Half-integer resonance caused by dc injection bump magnets and superperiodicity restoration in high-intensity hadron synchrotrons. Phys. Rev. Accel. Beams **26**, 104201 (2023). https://doi.org/10.1103/PhysRevAccelBeams.26.104201
11. J. Qiang, Bunched beam envelope instability in a periodic focusing channel. J. Phys: Conf. Ser. **1067**, 062015 (2018). https://doi.org/10.1088/1742-6596/1067/6/062015
12. Z.H. Li, P. Cheng, H.P. Geng et al., Physics design of an accelerator for an accelerator-driven subcritical system. Phys. Rev. ST Accel. Beams **16**, 080101 (2013). https://doi.org/10.1103/PhysRevSTAB.16.080101
13. D.O. Jeon, Classification of space charge resonances and instabilities in high-intensity linear accelerators. J. Korean Phys. Soc. **72**, 1523–1530 (2018). https://doi.org/10.3938/jkps.72.1523
14. A. Pathak, S. Krishnagopal, Higher order mode beams mitigate halos in high intensity proton linacs. Phys. Rev. Accel. Beams **20**, 014201 (2017). https://doi.org/10.1103/PhysRevAccelBeams.20.014201
15. M.A. Plum, Beam Loss in Linacs (2016). https://doi.org/10.48550/arXiv.1608.02456
16. M.A. Plum, Beam loss mechanisms in high-intensity linacs, in *Proceedings of ICFA Advanced Beam Dynamics Workshop on High-Intensity and HighBrightness Hadron Beams*. (JACoW Publishing, 2012), p.36 https://api.semanticscholar.org/CorpusID:195822960
17. R.A. Jameson, Beam-intensity limitations in linear accelerators. IEEE T. Nucl. Sci **28**, 2408–2412 (1981). https://doi.org/10.1109/TNS.1981.4331708
18. X.M. Wan, X.J. Pu, Z.Q. Ren et al., Discussion of 90 stopband in low-energy superconducting linear accelerators. Nucl. Sci. Tech. **33**(9), 121 (2022). https://doi.org/10.1007/s41365-022-01104-z
19. R.A. Jameson, An approach to fundamental study of beam loss minimization. Paper Presented at the AIP Conference Proceedings. American Institute of Physics **480**, 21–30 (1999). https://doi.org/10.1063/1.59501
20. B.L. Qian, J. Zhou, C. Chen, Image-charge effects on the envelope dynamics of an unbunched intense charged-particle beam. Phys. Rev. ST Accel. Beams. **6**, 014201 (2003). https://doi.org/10.1103/PhysRevSTAB.6.014201
21. T.P. Wangler, K.R. Crandall, R. Ryne et al., Particle-core model for transverse dynamics of beam halo. Phys. Rev. ST Accel. Beams **1**, 084201 (1998). https://doi.org/10.1103/PhysRevSTAB.1.084201
22. J. Qiang, Three-dimensional envelope instability in periodic focusing channels. Phys. Rev. Accel. Beams **21**, 034201 (2018). https://doi.org/10.1103/PhysRevAccelBeams.21.034201
23. K. Batygin et al., Chaotic dynamics driven by particle-core interactions. Phys. Plasmas **28**, 09310 (2021). https://doi.org/10.1063/5.0056306
24. J. Qiang, R.D. Ryne, Beam halo studies using a three-dimensional particle-core model. Phys. Rev. ST Accel. Beams **73**, 1247 (2000). https://doi.org/10.1103/PhysRevSTAB.3.064201
25. C. Li, Q. Xin, H. Yuan et al., Particle orbits in quadrupole-duodecapole halo suppressor. Nucl. Instrum. Meth. A **770**, 169–176 (2015). https://doi.org/10.1016/j.nima.2014.09.085
26. Y.K. Batygin, Analytical treatment of particle–core interaction. Nucl. Instrum. Meth. A **618**, 37–42 (2010). https://doi.org/10.1016/j.nima.2010.02.125
27. H.J. Yu, J.Q. Weng, L. Bai, Simulation on control of beam halo-chaos by power function in the hackle periodic-focusing channel. Nucl. Sci. Tech. **19**(6), 325–328 (2008). https://doi.org/10.1016/S1001-8042(09)60012-9
28. M. Ikegami, Particle-core analysis of beam halo formation in anisotropic beams. Nucl. Instrum. Meth. A **435**, 284 (1999). https://doi.org/10.1016/S0168-9002(99)00565-3
29. M. Ikegami, Particle-in-cell simulation study on halo formation in anisotropic beams. Nucl. Instrum. Meth. A **345**, 454 (2000). https://doi.org/10.1016/S0168-9002(00)00474-5
30. C. Li, Q. Qin, R.A. Jameson et al., Space charge induced collective modes and beam halo in periodic channels. Paper Presented at the 7th Int. Particle Accelerator Conf. (IPAC'16), Busan, Korea, 8–13 May (2016)
31. Linear beam optics with space charge: Sections 4.1 - 4.4, in Theory and Design of Charged Particle Beams (Wiley, 2008) Chap. 4, pp. 163–232
32. F.J. Sacherer, Rms envelope equations with space charge. IEEE T. Nucl. Sci **18**, 1105–1107 (1971). https://doi.org/10.1109/TNS.1971.4326293
33. J.M. Lagniel, Chaotic behaviour and halo formation from 2D space charge dominated beams. Nucl. Instrum. Meth. A **345**, 405 (1994). https://doi.org/10.1016/0168-9002(94)90490-1
34. T.M.C. Silva, R. Pakter, F.B. Rizzato et al., Halo formation and emittance growth in the transport of spherically symmetric mismatched bunched beams. Phys. Plasmas **22**, 023102 (2015). https://doi.org/10.1063/1.4907198
35. R.L. Gluckstern, A.V. Fedotov, S. Kurennoy et al., Halo formation in three-dimensional bunches. Phys. Rev. E **58**, 4977 (1998). https://doi.org/10.1103/PhysRevE.58.4977
36. Yu. Senichev, N. Vasyukhin, Hamiltonian formalism for halo investigation in high-intensity beams. Nucl. Instrum. Meth. A **561**, 166 (2006). https://doi.org/10.1016/j.nima.2006.01.020
37. R.L. Gluckstern, Analytic model for halo formation in high current ion Linacs. Phys. Rev. Lett. **73**, 1247 (1994). https://doi.org/10.1103/PhysRevLett.73.1247

38. M. Aslaninejad, I. Hofmann, Effect of space charge on linear coupling and gradient errors in high-intensity rings. Phys. Rev. ST Accel. Beams **6**, 124202 (2003). https://doi.org/10.1103/PhysRevSTAB.6.124202
39. M. Ikegami, S. Machida, T. Uesug, Particle-core analysis of dispersion effects on beam halo formation. Phys. Rev. ST Accel. Beams **2**, 124201 (1999). https://doi.org/10.1103/PhysRevSTAB.2.124201
40. Y.S. Yuan, G. Franchetti, Coherent dispersion effects in 2D and 3D high-intensity beams. Phys. Plasmas **30**, 123103 (2023). https://doi.org/10.1063/5.0167535
41. M. Venturini, M. Reiser, RMS envelope equations in the presence of space charge and dispersion. Phys. Rev. Lett. **81**, 96 (1998). https://doi.org/10.1103/PhysRevLett.81.96
42. S.Y. Lee, H. Okamoto, Space charge dominated beams in synchrotrons. Phys. Rev. Lett. **80**, 5133 (1998). https://doi.org/10.1103/PhysRevLett.80.5133
43. H.C. Chao, S.Y. Lee, Simulations of beam envelope dynamics in circular accelerators. Phys. Rev. ST Accel. Beams **18**, 024202 (2015). https://doi.org/10.1103/PhysRevSTAB.18.024202
44. "Sections 6-5-3" in *Computer simulation using particles* (RW Hockney and JW Eastwood, 1988), Chap. 6, pp. 208-214
45. S. Cousineau, S.Y. Lee, J.A. Holmes et al., Space charge induced resonance excitation in high intensity rings. Phys. Rev. ST Accel. Beams **6**, 034205 (2003). https://doi.org/10.1103/PhysRevSTAB.6.034205
46. D. Jeon, K.R. Hwang, J. Jang et al., Sixth-order resonance of high-intensity linear accelerators. Phys. Rev. Lett. **114**, 184802 (2015). https://doi.org/10.1103/PhysRevLett.114.184802
47. D. Jeon, L. Groening, G. Franchetti et al., Fourth order resonance of a high intensity linear accelerator. Phys. Rev. ST Accel. Beams **12**, 054204 (2009). https://doi.org/10.1103/PhysRevSTAB.12.054204
48. C. Li, R.A. Jameson, Structure resonances due to space charge in periodic focusing channels. Phys. Rev. Accel. Beams **21**, 024204 (2018). https://doi.org/10.1103/PhysRevAccelBeams.21.024204
49. Z.C. Liu, C. Li, Q. Qin, Structure resonance crossing in space charge dominated beams. Phys. Plasmas **26**, 5 (2019). https://doi.org/10.1063/1.5061774
50. D.O. Jeon, J. Jang, H. Jin, Interplay of space charge fourth order resonance and envelope instability. Nucl. Instrum. Meth. A **832**, 43–50 (2016). https://doi.org/10.1016/j.nima.2016.06.036
51. J.A. Holmes, V.V. Danilov, J.D. Galambos et al., Space charge dynamics in high intensity rings. Phys. Rev. ST Accel. Beams **2**, 114202 (1999). https://doi.org/10.1103/PhysRevSTAB.2.114202
52. H.S. Chen, X.L. Wang, China's first pulsed neutron source. Nat. Mater. **15**(7), 689–691 (2016). https://doi.org/10.1038/nmat4655
53. J. Wei, H. Chen, Y. Chen et al., China spallation neutron source: design, R &D, and outlook. Nucl. Instrum. Meth. A **600**, 10 (2009). https://doi.org/10.1016/j.nima.2008.11.017